A Proton Magnetic Resonance Study of the One Dimensional Antiferromagnetic System $CsFeCl_3 \cdot 2H_2O$

by

Michael J. Rensing
B.Sc., University of Victoria, 1982
M.Sc., University of Toronto, 1984

A Dissertation Submitted in Partial Fulfillment of the
Requirements for the Degree of

DOCTOR OF PHILOSOPHY

in the Department of Physics and Astronomy

We accept this dissertation as conforming to the required standard

Dr. A. Watton, Supervisor (Department of Physics and Astronomy)

Dr. H.W. Dosso, Departmental Member (Department of Physics and Astronomy)

Dr. R.M. Clements, Departmental Member (Department of Physics and Astronomy)

Dr. K.R. Dixon, Outside Member (Department of Chemistry)

Dr. D.E. Hewgill, Outside Member (Department of Mathematics)

Dr. E.D. Rogak, Additional Member (Department of Mathematics)

Dr. H. Peemoeller, External Examiner (University of Waterloo)

Supervisor: Dr. Arthur Watton

Abstract

Proton line shapes and spin-lattice relaxation times were acquired for the easy-axis antiferromagnet $CsFeCl_3 \cdot 2H_2O$. The line shapes were acquired at 250 K for a complete 360° rotation about the *b* axis of the crystal, and at various temperatures between 250 K and 23 K, for two orientations.

A model for the line shapes has been created based on the temperature dependance of the interaction between protons and the local magnetic field differences at each proton site. The field differences lead to symmetric line shapes whose peaks have a separation which increases as the temperature decreases. This model accounts well for the major component of the observed line shapes, provided that the proton-proton separation is increased over the separation obtained from published data. The residual portion of the observed line shapes appears to be a single line which results from water molecules which behave as though they are not part of the crystal structure.

A simple stochastic model for the behavior of π-kink solitons has been developed and used to predict values for the proton spin-lattice relaxation times. In this model, the solitons are treated as infinitesimal non-interacting particles travelling along straight chains of Fe^{2+} ions at constant speed. The arrival of solitons at a randomly chosen point on the chain is a Poisson process which leads to an expression for the spin-lattice relaxation whic agrees well with observations.

Examiners:

Dr. A. Watton, Supervisor (Department of Physics and Astronomy)

Dr. H.W. Dosso, Departmental Member (Department of Physics and Astronomy)

Dr. R.M. Clements, Departmental Member (Department of Physics and Astronomy)

Dr. K.R. Dixon, Outside Member (Department of Chemistry)

Dr. D.E. Hewgill, Outside Member (Department of Mathematics)

Dr. E.D. Rogak, Additional Member (Department of Mathematics)

Dr. H. Peemoeller, External Examiner (University of Waterloo)

Contents

List of Tables

List of Figures

List of Symbols

D ... magnetic anisotropy parameter

$G(\tau)$ ... correlation function

$\hbar$ ... Planck's constant divided by 2π

$\mathcal{H}_{chain}$ ... Hamiltonian of the iron spin system

$\mathcal{H}_z$ ... Zeeman Hamiltonian

$\mathbf{H_0}$ ... applied magnetic field

J, J_{ij} ... exchange integral

$J(\omega)$ ... spectral density

k ... Boltzmann's constant

$M(\tau)$ ... magnetization

r_{ij} ... inter-nuclear distance

$\mathbf{S}$, $\mathbf{S}_i$ ... nuclear spin vector

S_{ix}, S_{iy}, S_{iz} ... components of the i^{th} nuclear spin

T_1 ... nuclear spin-lattice relaxation time

β ... Bohr magneton

γ ... nuclear gyromagnetic ratio

λ ... arrival frequency of solitons

μ ... magnetic moment

ϕ_m ... canting angle of the iron magnetic moments

θ_{ij} ... angle between the inter-nuclear vector and the applied magnetic field

Acknowledgements

I would like to thank a number of people who have made it possible to complete this dissertation.

First, I have to thank my supervisor, Dr. Arthur Watton, for financial and moral support. Arthur always was encouraging, and our many discussions were always helpful.

Kathy Beveridge and Dr. Gordon Bushnell were of invaluable assistance by obtaining and analysing the X-Ray data of the crystals.

Neil Honkanen of the Physics and Astronomy Electronics Shop built and tested the Programmable Pulse Sequencer.

The text of this dissertation has been typeset using LaTeX on the Apollo computer system belonging to the University of Victoria High Energy Physics Group.

Chapter 1

Introduction

1.1 Magnetic Systems

Both ferromagnetic and antiferromagnetic materials are systems of magnetic spins arranged with some kind of order. The interaction between the spins which creates this order is known as the exchange interaction. The Heisenberg model for the exchange interaction between two spins i and j gives an energy

$$U = -2J_{ij}\mathbf{S}_i \cdot \mathbf{S}_j,$$

where J_{ij} is called the exchange integral, and is related to the overlap of the wave functions of the electrons on atoms i and j. Both ferromagnetic and antiferromagnetic systems can be described by this equation. For ferromagnetic systems, $J_{ij} > 0$, and the minimum energy configuration is then achieved when the spins all align parallel to each other. For antiferromagnetic systems, $J_{ij} < 0$, the minimum energy configuration is achieved when the spins are aligned in an antiparallel fashion, so that the net magnetic moment for the system is zero.

Some magnetic systems are more easily magnetized along certain axes than along others. The energy which causes this is called the anisotropy energy. One model which is used to describe systems with anisotropy is

$$U = D\sum_j S_{jz}^2,$$

where D is the anisotropy parameter. This can describe two types of system. If $D > 0$, the Hamiltonian is a minimum for $S_{jz} \rightarrow 0$, and we have an easy plane of magnetization. If $D < 0$, the Hamiltonian is minimum when S_{jz} is maximized, and we have an easy axis (the z axis, in this case). The term "easy plane" is used to describe a magnetic system whose magnetization is greatest when the applied field lies anywhere in a certain plane. The term "easy axis" is used to describe a magnetic system whose magnetization is greatest when the field is applied along one axis.

The magnetic system produces local fields which vary throughout the crystal. These local fields give rise to the fine structure of line shapes of nuclei within the crystal. This will be discussed in detail in Sec. 4.1.

There are a number of dynamic effects which reduce the order of perfectly aligned magnetic systems. One effect, whose quantization is known as a magnon, is caused by the motions of the spins in a wave. This is an oscillation of the relative orientation of the spins on a lattice. The term is analogous to the term phonon, used to describe the quantization of the oscillations of the atoms on a lattice. Since the magnons in a lattice are associated with changes in the spin orientations, they produce fluctuating fields within the crystal, which in turn can produce relaxation. Another excitation associated with the motion of the spins is the soliton. This is a non-linear disturbance which causes the orientation of the spins to change by large amounts over a relatively small distance. The motions of the solitons also produce fluctuating fields which can produce spin-lattice relaxation. Solitons will be discussed in Sec. 1.3.

1.2 $CsFeCl_3 \cdot 2H_2O$

The crystal $CsFeCl_3 \cdot 2H_2O$ belongs to the series of isomorphic transition-metal halides $AMB_3 \cdot 2aq$ (A = Cs,Rb; M=Mn,Co,Fe; B=Cl,Br; aq= H_2O, D_2O). A great deal of work has been done on $CsFeCl_3 \cdot 2H_2O$, and on the related compound $RbFeCl_3 \cdot 2H_2O$, to study Mössbauer line widths [Le Fever et al., 1981b], spin-cluster resonance [Nijhof

	300 K			4.2 K		
	x	y	z	x	y	z
Cs	$\frac{1}{4}$	0	0.1481(17)	$\frac{1}{4}$	0	0.1970(15)
Fe	0	0.4695(9)	$\frac{1}{4}$	0	0.4694(9)	$\frac{1}{4}$
$Cl_{(1)}$	$\frac{1}{4}$	$\frac{1}{2}$	0.1506(9)	$\frac{1}{4}$	$\frac{1}{2}$	0.1514(7)
$Cl_{(2)}$	0.0894(6)	0.2263(7)	0.3880(6)	0.878(4)	0.2267(6)	0.3893(6)
O	0.0680(10)	0.6864(14)	0.3650(12)	0.0681(15)	0.6829(10)	0.3684(10)
$D_{(1)}$	0.0262(11)	0.6873(13)	0.4404(11)	0.0267(8)	0.6882(11)	0.4424(8)
$D_{(2)}$	0.1716(12)	0.6903(13)	0.3842(11)	0.1721(10)	0.6962(11)	0.3817(9)
a		8.9809(7)Å			8.9466(6)Å	
b		7.2132(5)Å			7.1247(4)Å	
c		11.3867(10)Å			11.3245(10)Å	

Table 1.1: Structural parameters of $CsFeCl_3 \cdot 2D_2O$. The values for $CsFeCl_3 \cdot 2H_2O$ are assumed to be similar enough that these values can be used for theoretical calculations. 1σ standard deviations based on statistics only are given in parentheses, in units of the least significant digit. From Basten et al. [1978].

et al., 1983] [van Vlimmeren and de Jonge, 1979] [van Vlimmeren et al., 1980], specific heats [Kopinga, et al., 1985], neutron diffraction [Basten et al., 1978] [Smeets et al., 1985], and nuclear spin lattice relaxation times (T_1) [Tinus et al., 1982].

The crystallographic structure of $CsFeCl_3 \cdot 2H_2O$ belongs to the orthorhombic space group *Pcca* (D_{2h}^2), with the lattice parameters given in Table 1.1. There are four formula units per unit cell. The structure consists of *cis*-octahedra which are coupled along the *a* axis by a shared chlorine ion (Fig. 1.1). There is a strong exchange coupling between the neighbouring Fe^{2+} ions in this direction. The exchange interactions in the *b* and *c* directions are at least two orders of magnitude reduced from the exchange interaction in the *a* direction [Le Fever et al., 1981a]. This means that the system behaves as a quasi-one-dimensional magnetic system, so we can consider the Fe^{2+} system as chains of spins aligned along the *a* axis. The chains of magnetic Fe^{2+} ions are separated in the *b* direction by layers of Cs^+ ions. In the *c* direction the chains are separated by layers of water molecules.

The magnetic structure of $CsFeCl_3 \cdot 2H_2O$ exhibits long range order at a Néel

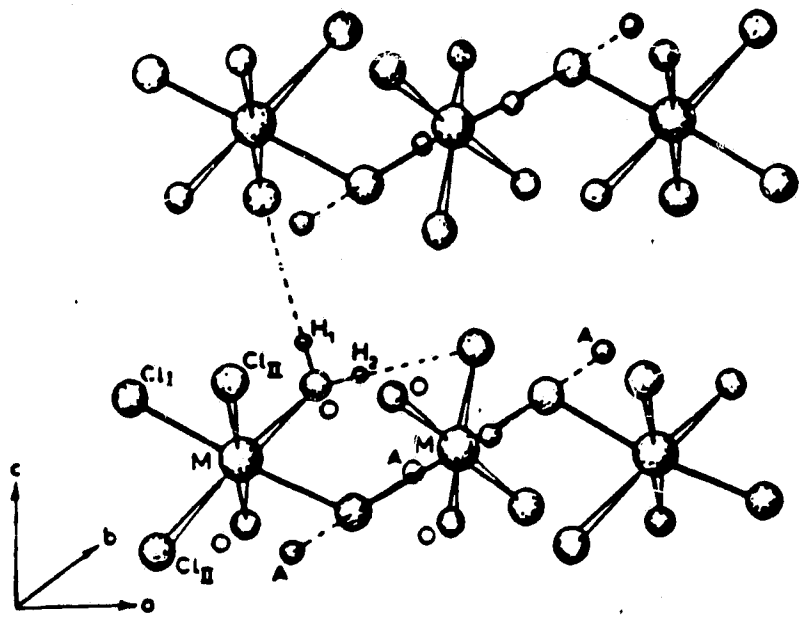

Figure 1.1: Schematic representation of the crystallographic structure. This is the general structure of $AMB_3 \cdot 2H_2O$. In this case, A = Cs, M = Fe, and B = Cl. Only one set of hydrogens and hydrogen bonds is shown. (From Le Fever et al. [1981a])

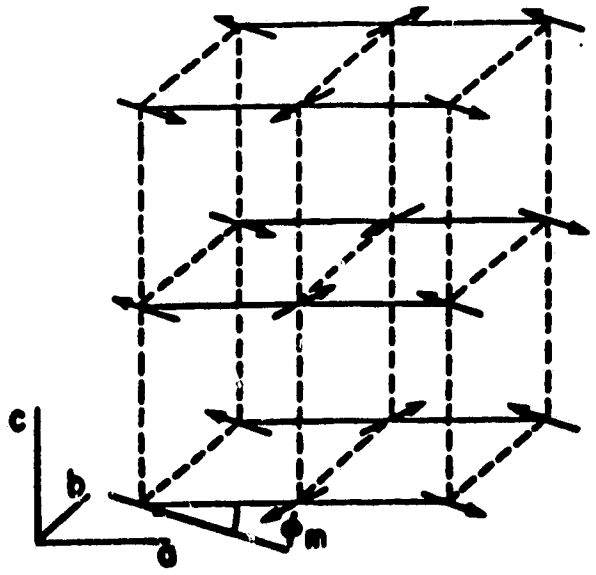

Figure 1.2: Array of the magnetic moments of $CsFeCl_3 \cdot 2H_2O$ in the ordered state. All moments are located in the ac plane at the canting angle ϕ_m from the a axis. (From Basten et al. [1978])

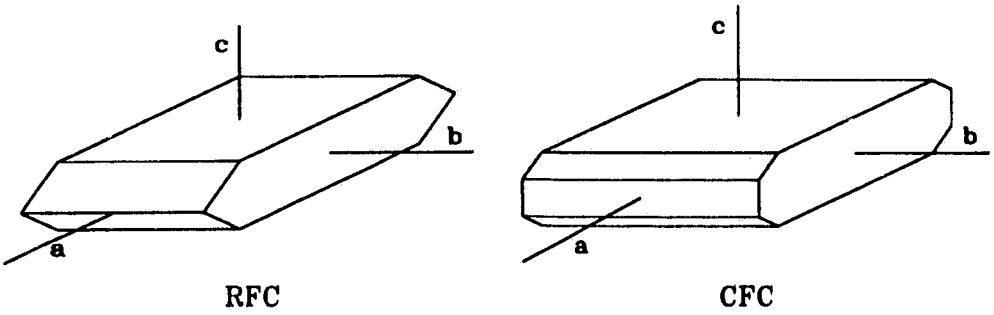

Figure 1.3: Morphology of single crystals. The $RbFeCl_3 \cdot 2H_2O$ (RFC) crystal shape is from Le Fever et al. [1981b], while the $CsFeCl_3 \cdot 2H_2O$ (CFC) crystal shape is the observed shape of our crystal.

temperature of $T_N = 12.6$ K [Le Fever et al., 1981b]. For the temperature range in which all of these experiments were conducted (30 K to 300 K), the crystal is paramagnetic, with the magnetic moments arranged as in Fig. 1.2. The spins do not align along a principal axis. Instead, they lie in the *ac* plane at a constant canting angle ϕ_m from the *a* axis. This will have the effect of reducing the symmetry so that the magnetic symmetry will be near to *Pcca*, but is expected to deviate somewhat. The canting angle is $\phi_m = 15°$ for $CsFeCl_3 \cdot 2H_2O$ [Basten et al., 1978]. This canting angle means that each antiferromagnetic chain has a net ferromagnetic moment in the *c* direction, which is compensated by the moments of neighbouring chains.

Fig. 1.3 shows the morphology of a single crystal of $RbFeCl_3 \cdot 2H_2O$, as well as the observed morphology of our single crystal of $CsFeCl_3 \cdot 2H_2O$. The similarity of the two types of crystal helped confirm the identification of the grown crystal.

1.3 Solitons

In the past thirty years, a great deal of interest has been generated in non-linear systems. These systems exhibit stable disturbances which have the following properties [Drazin 1983]:

1. The disturbance is localized.
2. The disturbance exists without dispersion, i.e. the disturbance is permanent.
3. A number of disturbances interact so that after the interactions each disturbance retains its form, with only a phase shift to show that the interactions have occurred.

These properties have led to the coining of the word "soliton" as a descriptive name for this type of disturbance.

Physically, solitons can be observed in a number of situations. The first recorded observation of a soliton was that of a solitary wave of water in a canal. J. Scott Russell [1844] reported that in 1834 he observed a boat stop suddenly, which resulted in "a rounded, smooth and well-defined heap of water, which continued its course along the channel apparently without change of form or diminution of speed". Soliton behavior has since been observed in other shallow water systems, as well as in atmospheric systems.

Since solitons exhibit particle-like properties, they have been proposed as models for elementary particles. Indeed, a number of particle field theories have soliton solutions, but these solitons would have such large masses that they are not yet observable.

Of particular interest to us are antiferromagnetic systems of spins arranged in chains which do not interact strongly with neighbouring chains. Within the chains, the spins are coupled so that they form sequences of spins which alternate in alignment. Given certain assumptions, Mikeska [1980] has shown that the motion of the spins can be described by what is known as a sine-Gordon equation. If the orientation of the spins is described in terms of a field ϕ, then the sine-Gordon equation in one dimension is of the form

$$\frac{\partial^2 \phi}{\partial z^2} - \frac{1}{c^2}\frac{\partial^2 \phi}{\partial t^2} = m^2 \sin \phi$$

where c is the characteristic speed, and m is the mass. The soliton solutions of this equation are known as kink solitons because the orientation of the spins changes through π over a relatively small number of atomic spacings, creating a kink in the alignment of the spins.

1.4 Motivation

This study was undertaken because there were no studies of the proton line shapes of $CsFeCl_3 \cdot 2H_2O$, and it was felt that such a study combined with T_1 measurements would add to the understanding of the interactions within the crystal. It was hoped that the soliton model for relaxation times [Mikeska, 1980] [Tinus et al., 1982] could be expanded, and that this model could be tested further by comparing it to the magnon model [Goto and Yan aguchi, 1981].

Since protons have spin $S = 1/2$, there are no quadrupolar interactions. This would have made the analysis of the line shapes extremely complex. The lack of possible quadrupolar interactions simplifies the problem by limiting the possible interactions to dipolar types of interactions. Another advantage to observing protons is that they are the nuclei which give the largest NMR response, which is of great use in obtaining data with a good signal to noise ratio in a reasonable experimental time.

Chapter 2

Experimental Methods

2.1 Growing the Crystals

The crystals of $CsFeCl_3 \cdot 2H_2O$ were grown by slow evaporation of a solution of CsCl and $FeCl_2 \cdot 5H_2O$ dissolved in distilled water [Basten et al., 1978] [Smeets et al., 1985]. The solutions were kept in an enclosed chamber filled with nitrogen to prevent formation of iron oxides, which precipitate from the solution.

Several days after the solutions were first mixed, small crystals began to appear. These were allowed to grow until crystals of about one millimetre in the smallest dimension appeared. The most regular shaped of the crystals were then removed from the solutions and kept for seed stock to grow larger crystals.

Some of the seed stock crystals were sent to a commercial laboratory for chemical analysis, and proved to have too little chlorine for the correct stoichiometry. Also, a large number of these crystals did not conform to the description of the macroscopic shape given by Le Fever et al. [1981b], and a brief X-Ray analysis using a Nonius CAD 4-F diffractometer showed that these crystals were triclinic. These crystals were dissolved in distilled water and allowed to form "second generation" crystals, again by slow evaporation. The new crystals did conform to the macroscopic shape described by Le Fever et al. (see Fig. 1.3). Leaving the crystals to grow larger on the bottom of the beakers merely resulted in large masses of small crystals growing randomly on

	Measured	Expected
a	8.94(3)Å	8.9809(7)Å
b	7.196(3)Å	7.2132(5)Å
c	11.346(9)Å	11.3867(10)Å
α	90°.22(5)	90°
β	90°.12(15)	90°
γ	90°.18(12)	90°

Table 2.1: X-Ray analysis of the crystal structure of $CsFeCl_3 \cdot 2H_2O$. Expected values are from Basten et al. [1978]. 1σ standard deviations based on statistics only are given in parentheses, in units of the least significant digit. The measured values are based on a poor quality crystal. They are accurate enough to confirm the identity of the crystal, but were not used in any calculations.

each other.

All of the clean crystals from the "second generation" solutions were kept until a large enough supply was obtained to allow them to be re-dissolved in distilled water and produce a useful volume of solution from which more crystals can be grown. Samples of the "second generation" crystals were sent for chlorine analysis, and proved to have the correct percentage of chlorine. An X-ray analysis was performed on a Nonius CAD 4-F diffractometer. A unit cell structure was determined using the routine SEARCH, after which a transformation of the unit cell into meaningful parameters was done using the routine TRANS. The final results agreed well with the published parameters (see Table 2.1), confirming the identity of the crystal.

A later X-Ray analysis using a Weissenberg rotation photograph was not completely successful, but it did confirm that the principal axes of the crystal were perpendicular to the crystal faces. Attempts were made to cleave the crystal along the macroscopic crystal axes. Only one plane proved to have easy cleavage, agreeing with Smeets et al. [1985], and van Vlimmeren and de Jonge [1979].

A concentrated liquor was obtained by dissolving the small "second generation" crystals, and seed crystals were suspended from a thread in the liquor. The seed crystals in the "third generation" solutions were allowed to grow for several months,

while the solutions were filtered and more "third generation" solution was added as required. Only one crystal grew successfully from four starting seeds, but this one reached dimensions of roughly $6\times3\times1$ cm^3 . One other crystal reached dimensions of roughly $1\times0.5\times0.5$ cm^3 before it would not continue to grow consistently. This proved to be an excellent test crystal for the preliminary work.

A few preliminary experiments were performed using this test crystal, in order to determine tuning procedures and experimental parameters. These experiments produced preliminary line shapes which had the symmetry expected for a reduced symmetry *Pcca* structure (see Sec. 4.1.1). Also, preliminary T_1 measurements agreed with the results published by Tinus et al. [1982].

To summarize, the results from a number of tests confirmed that the crystals were $CsFeCl_3{\cdot}2H_2O$:

1. The morphology of the crystals of $CsFeCl_3{\cdot}2H_2O$ agreed with published descriptions of the isomorphic crystal $RbFeCl_3{\cdot}2H_2O$. This was a good indication that the crystal had the same basic structure as $RbFeCl_3{\cdot}2H_2O$, as it should have had.

2. The crystals cleaved easily along only one plane, agreeing with Smeets et al. [1985], and van Vlimmeren and de Jonge [1979]. If we oriented the crystal on the basis of Le Fever et al.'s picture, the direction of cleavage was along the *ab* plane, again agreeing with these authors' descriptions.

3. The X-Ray analysis produced lattice parameters which agreed with the published data.

4. The chemical analysis gave a chlorine content which agreed with the expected content for $CsFeCl_3{\cdot}2H_2O$.

5. CW experiments indicated that the line shapes followed the patterns expected for $CsFeCl_3{\cdot}2H_2O$ when the orientation was changed.

6. Pulse NMR experiments (see Sec. 3.2) gave T_1 values which agreed well with those of Tinus et al. [1982].

It was found that the crystalline structure was quite easy to destroy. Drying a crystal by enclosing it in a container over a desiccant, by placing it in a vacuum, or by blowing dry nitrogen gas over it all caused the crystal to become an opaque yellow colour. When the opaque crystals were cut open after a short drying time, it was found that the interiors were still clear, and apparently crystalline. Longer drying times produced crystals which were opaque throughout. CW experiments were performed on these crystals before and after drying. The line shapes from the crystal showed definite structure before drying, whereas after complete drying of the crystal, only one narrow line was observed, indicating that the crystalline structure was destroyed by the drying process.

2.2 CW Experiments

Proton line shapes for $CsFeCl_3 \cdot 2H_2O$ were obtained using a Spin-Lock MO-100 marginal oscillator operating at 30 MHz. The resonant magnetic field was applied by a Varian electromagnet. A low level 100 Hz magnetic field was added to the resonant field by a pair of Helmholtz coils. This caused a modulation at the same frequency in the response from the sample. This response was used as input to an Ithaco Dynatrac 391A lock-in amplifier, which detected and filtered the signal. Because of the modulation field, the signal measured was actually the derivative of the line shape centred about the time average of the total applied field. The signal was recorded using two different systems.

The preliminary data were recorded using an eight-bit analogue to digital converter interfaced to a PC-XT. The computer would record several scans, and store them on disk. As there was concern that there would be some drift in the field at which the scans would begin, the experimenter would align the scans using some clearly defined

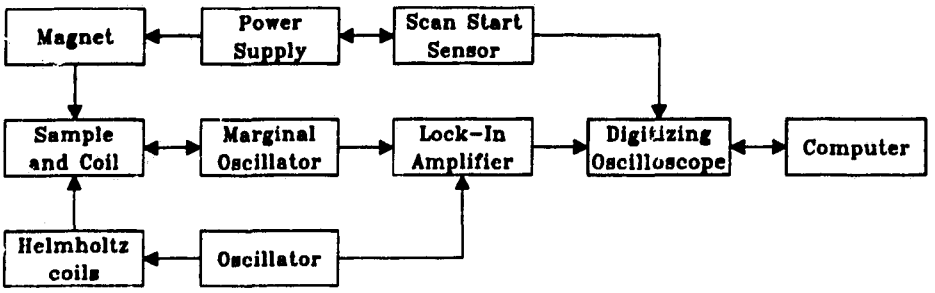

Figure 2.1: Block diagram of the CW experiment apparatus.

feature of the derivative line shape. The computer would then average the data and store it on disk.

The final data were recorded using the Tektronix 2230 Digital Storage Oscilloscope. An accurate trigger was built to detect the start of each scan, and the oscilloscope external clock function was used. The Programmable Pulse Sequencer (see Appendix A) was used to generate an external time base for the oscilloscope, so that each scan of the magnetic field corresponded to one scan of the oscilloscope. At the end of each scan, the derivative line shape data were read from the oscilloscope and stored on a magnetic disk. At some later time, the experimenter would use a computer program to align and sum the scans, and then integrate the derivative line shape to produce the actual line shape. A block diagram of the experimental setup is shown in Fig. 2.1.

Using the test crystal, proton line shapes were obtained with the applied magnetic field in the *ac* plane. The crystal was rotated about the *b* axis, and a line shape was obtained every ten degrees for 360 degrees starting from an arbitrary orientation (Fig. 2.2). The symmetries observed (see Sec. 4.1.1) agreed with the expected behavior for the theoretical line shapes of $CsFeCl_3 \cdot 2H_2O$, supporting our identification of the structure.

Several experiments were performed by reversing the direction of the scan to confirm that there were no distortions of the line shapes resulting from the scan

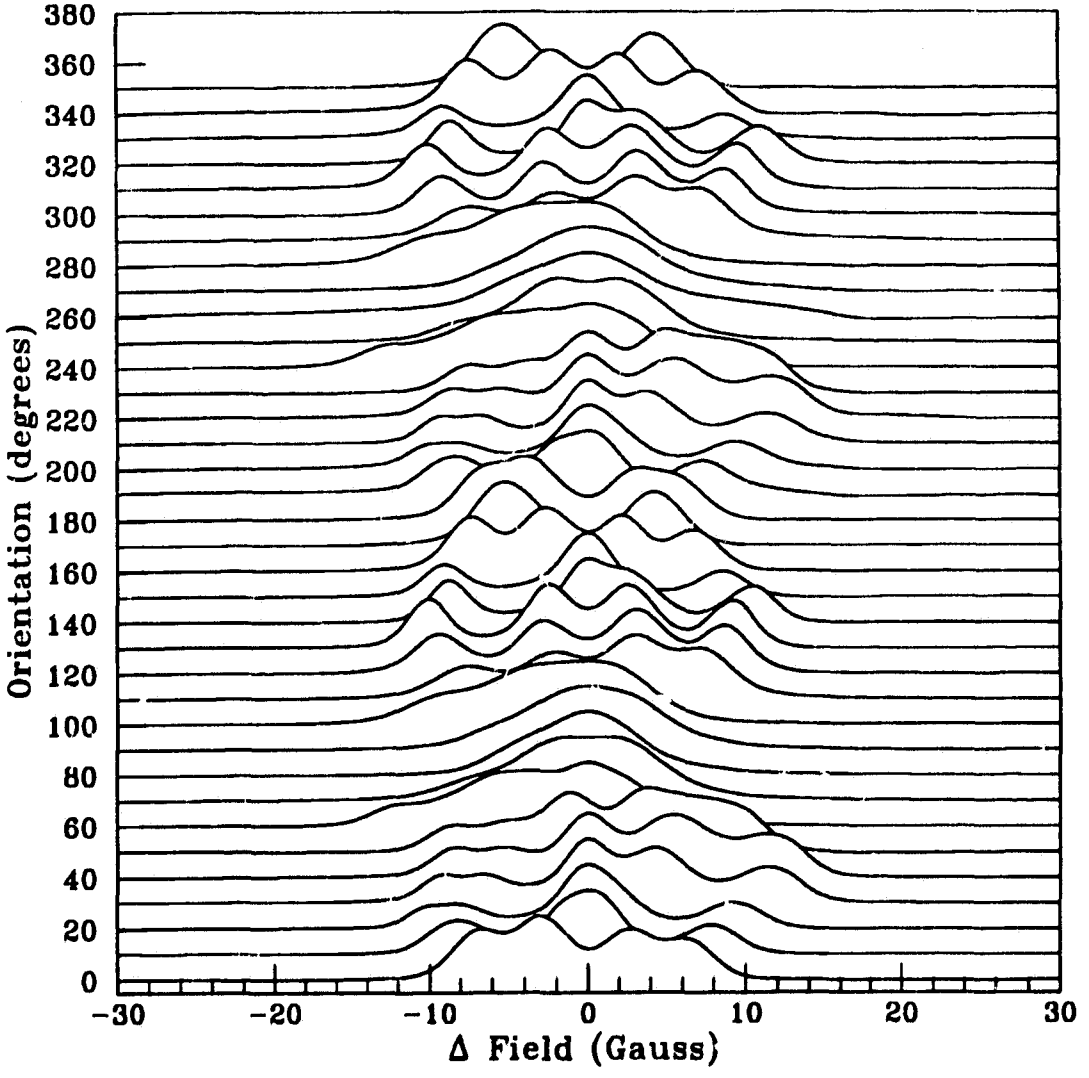

Figure 2.2: The observed line shapes. The orientations are relative to an arbitrary 0° orientation. The line shape baseline corresponds to the orientation, while the amplitude is in arbitrary units.

direction. No such distortions were observed.

To ensure that the rate of change of the magnetic field did not cause distortions of the line shape, the scan rate was increased until distortions were observed. The scan rate used was one order of magnitude less than the rate at which the distortion first appeared. A similar method was used to ensure that the filtering time constant did not introduce distortions. The time constant was increased until distortions were observed. The time constant used was one order of magnitude less than the value for which the distortions were first observed. These checks were performed before beginning the acquisition of each line shape.

Once a number of preliminary experiments had been performed on the small sample crystal to determine some of the experimental parameters and procedures, a sample was cut from the large crystal so as to allow the sample to be rotated about the *b* axis. X-Ray back scattering confirmed that the sample was cut so that the sample could be aligned to within 5° of the *b* axis, but it was not possible to shape the crystal in order to orient it more precisely, because of its brittle nature. A large enough piece of the crystal survived the attempt at shaping to be an excellent sample for further experimental study. Unfortunately, the small test crystal used previously, which was also an excellent sample, was destroyed in an attempt to remove unattached water molecules. These were suspected to be present on the surface and at defect sites in the crystal because of otherwise unexplained features in the observed line shapes. (see Sec. 3.1 and 4.1.4)

Line shapes were obtained from the cut sample for a temperature range of 250 K to 23 K. At 23 K the signal disappeared. This disappearance can probably be attributed to the signal broadening enough for the intensity to fall below the noise level of the spectrometer. The discussion of the CW line shapes will be continued in Sec. 3.1.

2.2.1 Calculating the Line Shapes

In order to observe the line shapes directly, the derivative line shapes were integrated using the formula

$$Y_n = \frac{\Delta}{2}\left(\frac{y_1}{2} + \sum_{i=2}^{n-1} y_i - \sum_{i=n+1}^{N-1} y_i - \frac{y_N}{2}\right), \tag{2.1}$$

where Δ is the spacing between consecutive points in the data, and N is the number of points in the derivative line shape. When y_i goes to zero at $\pm\infty$, this is equivalent to

$$Y_n = \Delta\left(\frac{y_1}{2} + \sum_{i=2}^{n-1} y_i + \frac{y_n}{2}\right). \tag{2.2}$$

Eq. (2.1) was used instead of the more usual Eq. (2.2) because the noise in the signal causes the error in Y_n calculated from Eq. (2.2) to increase as n increases. If Eq. (2.2) was used, the baseline of the integrated line shape showed a definite slope because of the errors in the data points of the derivative line shape. The errors result from two sources; the random measurement errors, and the systematic errors resulting from the imprecision in the definition of the baseline. If Eq. (2.2) is used, the random errors create a random walk which manifests itself as an offset in the baseline of the integrated line shape. When Eq. (2.1) is used, the random walk problem is eliminated, the offset of the baseline of the integrated line shapes is greatly reduced, and the slope of the baseline will be the result of the baseline imprecision of the derivative line shape only.

2.3 Pulse Experiments

Spin-lattice relaxation times (T_1) for the proton system in $CsFeCl_3{\cdot}2H_2O$ were obtained using a Spin-Lock coherent pulse spectrometer with a 30 MHz probe. A block diagram of the apparatus is shown in Fig. 2.3. The pulse sequences used were controlled by the Programmable Pulse Sequencer (PPS) described in Appendix A. The

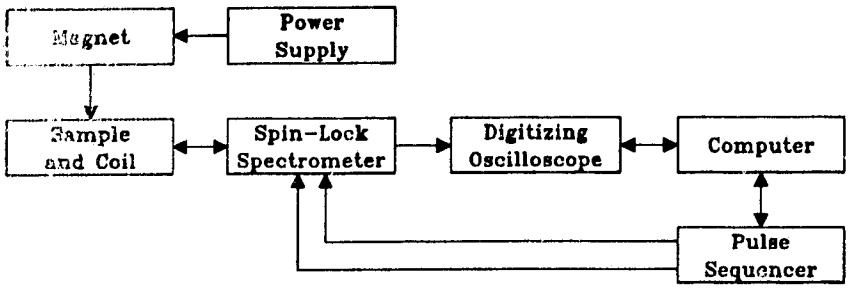

Figure 2.3: Block diagram of the pulse experiment apparatus.

free induction decay (FID) data were recorded using a Tektronix 2230 Digital Storage Oscilloscope.

The signals were detected using the diode detect mode instead of the phase detect mode. This meant that the signals were rectified, thereby improving the stability of the experiments by reducing the sensitivity of the system to small drifts in the magnetic field. This also eliminated the phase coherence information in the signal, simplifying the tuning procedure. The gain of the system was adjusted so that the signal was measured in the linear portion of the diode detector response curve. The dead time for the system was $6\mu s$.

It was decided that a $\frac{\pi}{2}$-τ-$\frac{\pi}{2}$ pulse sequence would be used to produce a magnetization recovery curve ($M(\tau)$) from which T_1 could be measured. (A $\frac{\pi}{2}$ pulse is a pulse which causes the magnetization in the rotating frame to rotate through an angle of $\frac{\pi}{2}$ radians.) The reason was that, because the measured values of T_1 were so short, a continuous $\frac{\pi}{2}$ pulse saturation sequence would not allow us to measure the FID baseline accurately. After some experimentation with pulse lengths, it was found that pulse lengths greater than $5\mu s$ introduced a distortion in the shape of the measured magnetization recovery curve. For this reason it was decided to use a pulse length of $5\mu s$. Shorter pulse lengths did not produce any measurable change in the magnetization recovery curve. This meant that the pulses used may have produced less than a $\frac{\pi}{2}$ rotation of the magnetization but because of the width of the resonance,

creating a $\frac{\pi}{2}$ pulse for all the spins was not possible anyway.

As a result of the complex nature of the proton line shapes, the FID curves of the protons were also complex. That is, they were not simple exponentials. Although there was some evidence that different parts of the FID relaxed with different time constants, the differences were so slight that it was impossible to separate any differences from the noise in the signals. It was decided to treat the entire FID as the response of a nuclear spin system relaxing to the lattice as an exponential with a single time constant, T_1. It was assumed that the pulse lengths were negligible with respect to the spin-spin relaxation time, so that there was no evolution of the spin system during the time that the pulses were applied. In other words, it was assumed that the magnitude of the magnetization did not change while the pulses were being applied.

The shorter-than-$\frac{\pi}{2}$ pulses produced a magnetization, measured immediately after the end of the second pulse, given by

$$M(\tau) = (M(\infty) - M(0))\left(1 - e^{-\tau/T_1}\right) + M(0)$$

where τ is the time between the two pulses, $M(\tau)$ is the measured magnetization, $M(\infty)$ is the equilibrium magnetization for the system, and $M(0)$ is the residual magnetization. If the pulses were exactly $\frac{\pi}{2}$, we would have $M(0) = 0$. T_1 is the spin-lattice relaxation time for the system.

It was found that the PPS, combined with the signal averaging capabilities of the digitizing oscilloscope, allowed measurements of T_1 to be made over a much larger range and to a greater accuracy than was previously possible. However, two problems immediately became apparent.

The first problem was a result of the discrete nature of the data from the oscilloscope. If the noise level of the averaged signal is low enough to be less than one digitization interval, the error is no longer normally distributed. Instead, the maximum error for each point is a constant equal to one digitization interval. This can

lead to problems when trying to estimate the overall error for parameters which have been determined using curve fitting routines, since these routines are used with the assumption that the errors in the data are distributed according to a normal distribution. After some study, this problem was ignored because the error was so small that no significant consequences occurred by assuming a normal distribution of errors.

A suggestion has been made that this problem could be circumvented by generating artificial electrical noise with known parameters and adding it to the signal being digitized. This method may be implemented if it becomes necessary, but to date it has not been used.

The second problem was much more significant. Until computer acquisition was added to the experimental procedure, the method of finding values for T_1 consisted of plotting the magnetization as a function of τ on semi-logarithmic paper, and then fitting a line by eye. This leads to a (visually) weighted fit, where the slope of the line was $1/T_1$. As a numerical fit is much more accurate, the computer was programmed to find T_1 automatically. This requires a more rigorous approach to the error analysis, so we will proceed as follows.

$M(\infty)$, $M(\tau)$, and $M(0)$ all have measurement errors associated with them, but the error in $M(\infty)$ and $M(0)$ will be constant and independant of τ for each measurement of T_1. $M(\tau)$, however, is remeasured for every value of τ. This means that the error in $M(\tau)$ is the only one which introduces an error which depends on τ. This could affect a least squares fit for T_1. If we write the error in $M(\tau)$ as ε_M, we have

$$\begin{aligned} y(\tau) = -\frac{\tau}{T_1} &= \ln\left[\frac{M(\infty) - M(\tau) \pm \varepsilon_M}{M(\infty) - M(0)}\right] \\ &= \ln\left(\left[\frac{M(\infty) - M(\tau)}{M(\infty) - M(0)}\right]\left[1 \pm \frac{\varepsilon_M}{M(\infty) - M(\tau)}\right]\right) \\ &= \ln\left[\frac{M(\infty) - M(\tau)}{M(\infty) - M(0)}\right] + \ln\left[1 \pm \frac{\varepsilon_M}{M(\infty) - M(\tau)}\right] \end{aligned}$$

$$\approx \ln\left[\frac{M(\infty)-M(\tau)}{M(\infty)-M(0)}\right] \pm \frac{\epsilon_M}{M(\infty)-M(\tau)},$$

where the last term is the portion of the error in $y(\tau)$ which depends on τ.

We can see that these errors are not constant for each value of τ, and that the errors in $M(\tau)$ should be weighted by $1/(M(\infty)-M(\tau))$ in order to obtain an accurate fit for $y(\tau)$. The weighting results in errors for $y(\tau)$ which do not have the same normal distribution. The least squares method used to make a linear fit to the data depends on all of the errors having the same normal distribution for different τ in order to calculate the variance in the fit. Even if the input errors are weighted to obtain the correct value for $1/T_1$, a correct value for the variance of $1/T_1$ will not be obtained. Because of the increased range of pulse spacings for which it was possible to make meaningful observations, this became a significant problem. Although the values for $1/T_1$ appeared to be accurately fitted, a visual examination of the plots of the data showed large deviations from the fitted line for long values of τ.

A data resampling scheme known as the jackknife fit (Appendix B) allows this problem to be avoided, but the visual fit is still not informative. For this reason it was decided to use a χ^2 fit to the un-transformed data. The actual curve fit to the data was

$$y = A[1]\left(1 - e^{-\tau/A[2]}\right) + A[3] \tag{2.3}$$

where $A[1] = (M(\infty) - M(0))$, $A[2] = T_1$, and $A[3] = M(0)$. This method has the benefit of producing a meaningful covariance matrix for the three parameters being found, as the errors of the input data have the same normal distribution for all τ. Also, as the errors should all have the same distribution, the visual fit of the plot shows any problems in the input data more clearly. Unfortunately, since the magnitude of the input error is not known, the actual variance of T_1 cannot be calculated from the fit, and the jackknife fit must still be used to get a realistic estimate of the error.

T_1 values were found for $CsFeCl_3{\cdot}2H_2O$ at various orientations and temperatures. The discussion of the T_1 data will be continued in Sec. 3.2.

2.4 Chapter Summary

- Two useful crystals of $CsFeCl_3 \cdot 2H_2O$ were grown. The small one was used as a test crystal for preliminary work. The large one was cut to provide the sample on which the major portion of this thesis is based.
- The identification of the crystals was confirmed by a number of methods.
- CW experiments were performed to obtain derivative line shapes at a number of orientations at 250 K, and at a number of temperatures for two orientations. The derivative line shapes were integrated using a numerical method which allowed for statistical errors in the data.
- Pulse experiments were performed to obtain proton spin-lattice relaxation times at a number of temperatures for two orientations.

Chapter 3

Experimental Results

3.1 CW Line Shapes

Immediately after the test crystal was grown, a few line shapes were acquired as described in Sec. 2.2, but without the digitizing recorder or signal averaging. The information obtained was enough to confirm that the crystal appeared to be a single crystal, and that the line shapes did have some structure. The crystal was then stored for about a year while the large crystal was grown, and the new data acquisition equipment was developed. When experiments were resumed, the new line shapes appeared to have been modified by the addition of another peak. The protons producing this peak were assumed to have been absorbed from the environment while the crystal was stored. This is why a number of attempts were made to dry the crystal. The water molecules containing the protons producing this additional peak will be referred to as "additional water". This will be discussed at a number of points in the following text.

3.1.1 The Orientation Dependance of the Line Shapes

The first set of line shapes were acquired from the test crystal as described in Sec. 2.2. The crystal was rotated about its b axis with the magnetic field applied in the ac plane. Line shapes were acquired every ten degrees starting from an arbitrary orientation.

The temperature was held at about 250 K since the oscillator would not operate above this temperature. The line shapes are shown in Fig. 2.2. From these line shapes, a number of observations can be made:

- The line shapes are quite complex, and can change dramatically over quite small ranges of orientation.

- There is a two-fold rotational symmetry, in that the line shapes 180° apart appear to be the same. The two-fold symmetry is predicted by the *Pcca* symmetry as a reduction of a four-fold reflection symmetry, but the full reflection symmetry is not apparent. This could be attributed to an internal magnetic field created by the canting of the spins as described in Sec. 1.2, which reduces the symmetry. Not enough data have been acquired to date to prove this, but if one examines Fig. 2.2 closely, one can see similarities in line shapes which indicate that the magnetic structure has near four-fold symmetry. This agrees with the fact that the canting angle is small.

- The number of peaks appearing in the line shapes varies between one (e.g. 80°) and five (e.g. 30°). While it is not surprising that there are orientations where an odd number of peaks is observed, it is surprising that the maximum number of peaks is odd. If there are no quadrupolar interactions (and there are none), the dipole-dipole interaction alone would produce pairs of peaks. These could blend together to produce an odd number of peaks, but it would be very improbable for the maximum number of peaks observed to be the result of such a blend. One explanation which is more plausible is the additional water further discussed in Sec. 4.1.4.

- An asymmetry can be observed in the line shapes. To verify that this was not an artifact of the experimental techniques, the direction of the magnetic field scan was reversed, and the equipment settings were checked. This asymmetry is of particular interest because, as will be shown later, the absorption line

shape should be symmetrical about the centre of the line. Again, a plausible explanation is the additional water discussed in Sec. 4.1.4.

The last two points are complications which indicated that the dependance of the line shapes on temperature would have to be studied next. Because of the great length of time which would have been required to repeat the orientation study at a number of different temperatures (each line shape requires ten hours), it was decided to limit the temperature experiments to three orientations:

1. The orientation for which the line profile is the simplest (a single peak). For reasons which will become apparent in the theory section, this was called the 0° orientation.

2. The orientation perpendicular to the 0° orientation, where the line shape has only two peaks. This was called the 90° orientation.

3. An orientation 27° from the two peaks orientation, where the next simplest line shape appears. This was called the 63° orientation.

3.1.2 The Temperature Dependance of the Line Shapes

The 0° orientation line shapes at various temperatures are plotted in Fig. 3.1. The single peak which was observed at 250 K first divided into two peaks of unequal amplitude as the temperature was decreased to about 215 K, then into three peaks as the temperature was decreased further. When three peaks were observed, the outer two were of nearly the same amplitude. At 32 K this pattern was similar, but the low field peak split into two on either side of the position where a single peak was expected. The 23 K line shape showed a single peak. The peak expected on either side had decreased in amplitude enough to be indistinguishable from the noise, and hence were unobservable. Because there were no other peaks present to provide reference positions, it was not possible to calculate the shift of this peak relative to its high

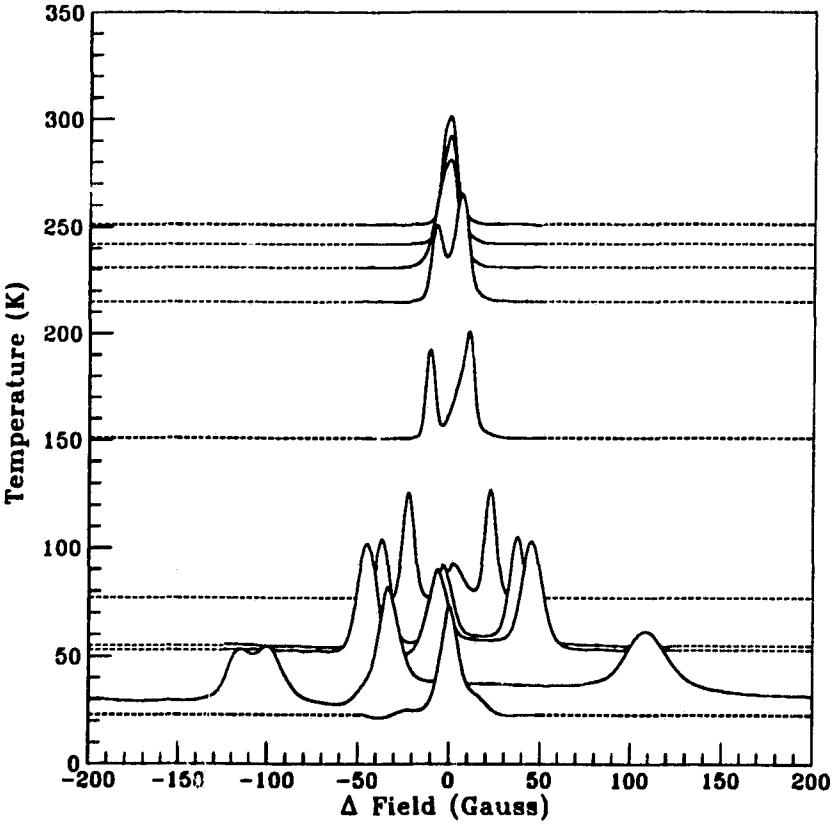

Figure 3.1: The 0° orientation line shapes. The baseline corresponds to the experimental temperature, while the amplitudes are in arbitrary units. The dashed portions of each line shape indicate data which were not recorded as part of the line shape.

temperature position. This is why it is plotted with zero field shift. Our theoretical explanation for these line shapes will be given in Sec. 4.1.

The 63° orientation line shapes are plotted in Fig. 3.2. The data were acquired only for temperatures above 77 K because it soon became apparent that this was a complex line shape as a result of the behavior of the internal magnetic fields, hence the study of this orientation was discontinued and has been left as a topic for future study.

The observed line shapes for the 90° orientation are shown in Fig. 3.3. There

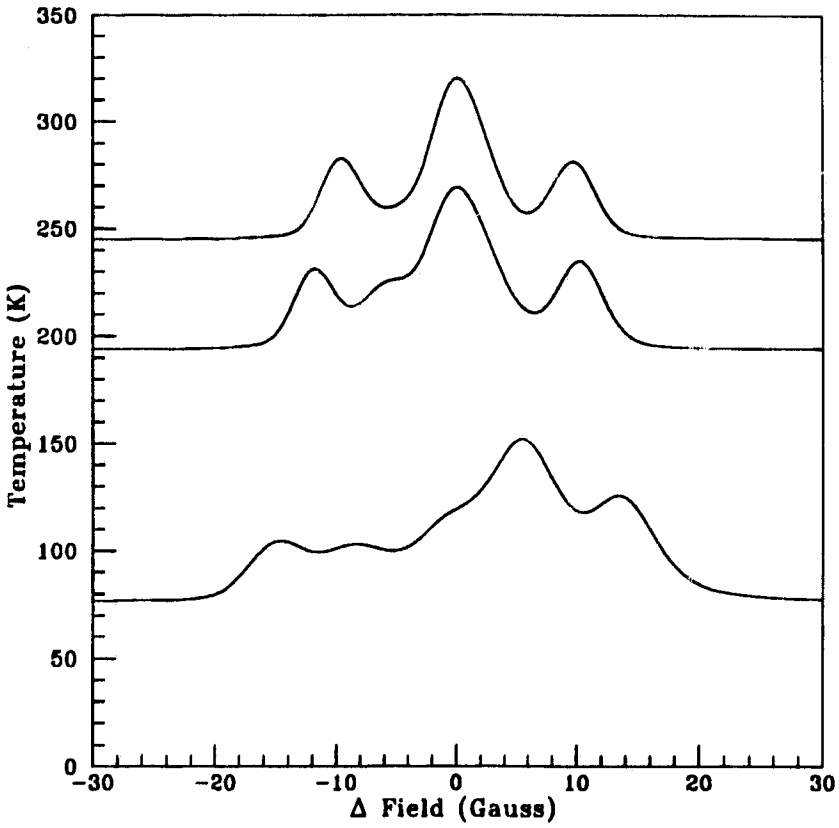

Figure 3.2: The 63° orientation line shapes. The baseline corresponds to the experimental temperature, while the amplitudes are in arbitrary units.

are no dramatic changes to the line shape over a large range in temperature. The main feature is that the difference between the amplitudes of the two peaks becomes greater as the temperature decreases. At the same time, the line is broadening, so the minimum between the two peaks is becoming less pronounced, until the line blends into one asymmetrical peak at 32 K. Our explanation for this behavior is given in Sec. 4.1.

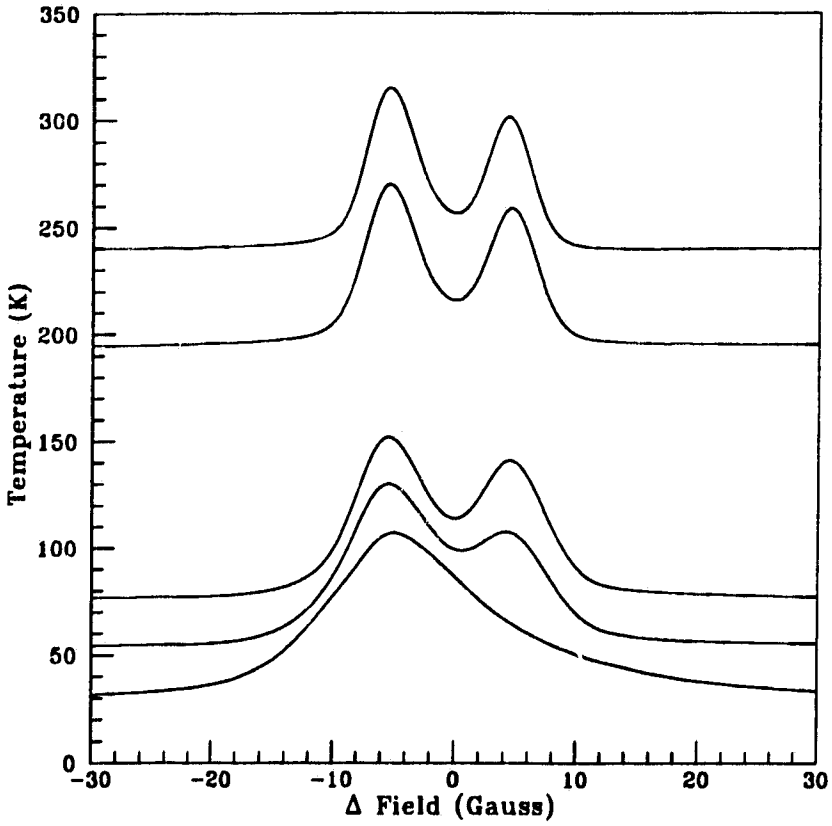

Figure 3.3: The 90° orientation line shapes. The baseline corresponds to the experimental temperature, while the amplitudes are in arbitrary units.

3.2 The T_1 Values

As with the CW line shapes, the T_1 values were acquired for the 0° and 90° orientations. The other orientations will be left for future study.

A series of measurements was made at the 0° orientation between 53.5 K and 294 K. Significant variations in T_1 were found at each temperature. Because of the spread in local fields, the signal response is spread over a range of magnetic field strengths. We will call this spread in the field strengths the signal response range. It was discovered that the variations in T_1 occurred as the field strength was varied

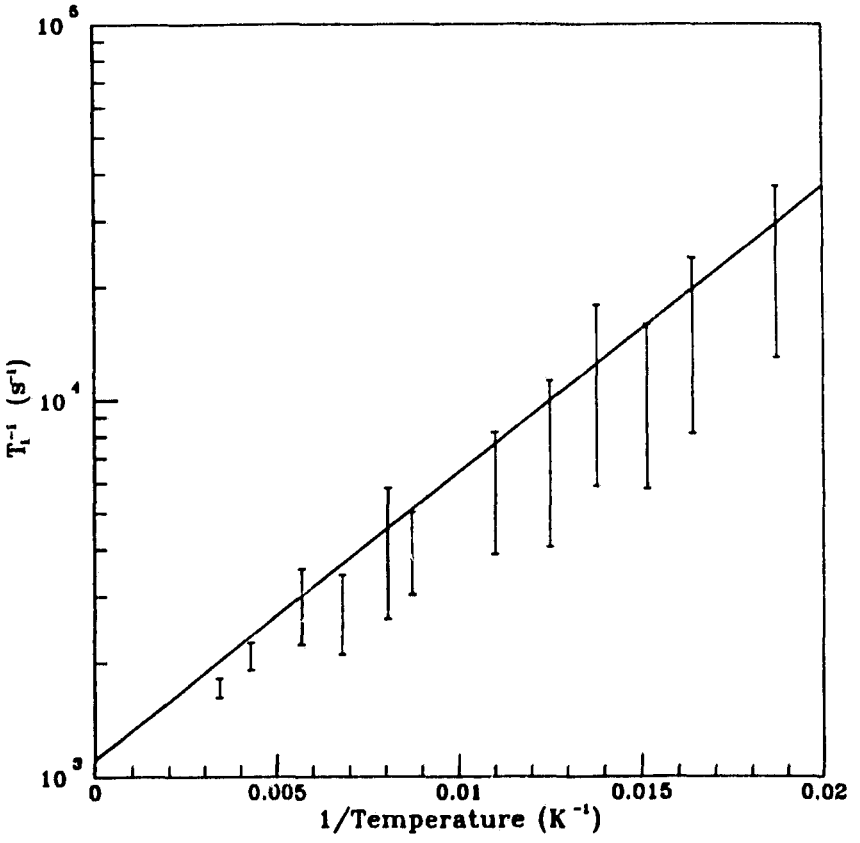

Figure 3.4: The T_1 data for the 0° orientation. The vertical bars are the range of T_1 values across the signal response range. The line is the theoretical curve predicted by the stochastic soliton model.

from one side of the signal response range to the other. As a result, measurements of T_1 were made at a number of points across the signal response range. The results of these experiments are plotted in Fig. 3.4 for the 0° orientation. A similar set of experiments was performed for the 90° orientation. The results are plotted in Fig. 3.5. In both plots, the bars at each temperature give the measured range of T_1 values for that temperature.

For both orientations, the measured values for T_1 agree well with those of Tinus et al. [1982]. It is to be noted that the range of T_1 values observed across the signal

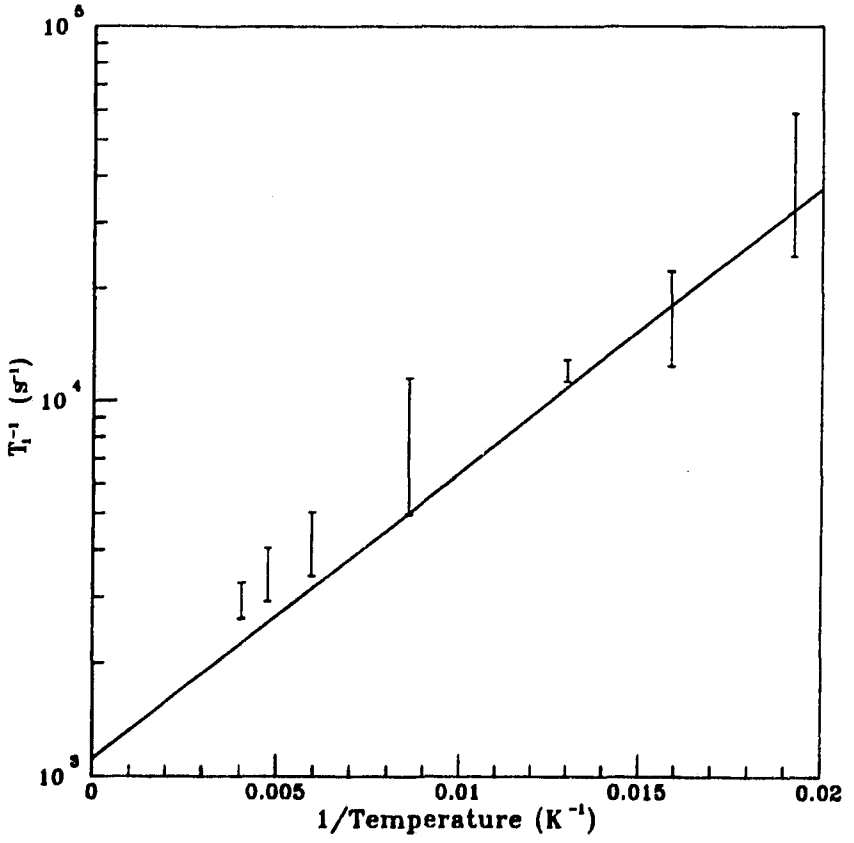

Figure 3.5: The T_1 data for the 90° orientation. The vertical bars are the range of T_1 values across the signal response range. The line is the theoretical curve predicted by the stochastic soliton model.

response range corresponds to the range of scatter present in the data of Tinus et al.. The theoretical explanation of these results is given in Sec. 4.2.

3.3 Chapter Summary

- With the test crystal at a temperature of 250 K, line shapes were acquired by rotating the crystal about its *b* axis, with the magnetic field in the *ac* plane.
- Line shapes were acquired for a number of temperatures between 250 K and

23 K for the 0°, 63°, and 90° orientations.

- Spin-lattice relaxation times were acquired for the 0° and 90° orientations at a number of temperatures between 53.5 K and 273 K.

Chapter 4

Theoretical Analysis and Discussion

4.1 The Line Shapes

To analyse the line shapes observed in the CW experiments, the interaction between two protons on the same water molecule will be studied Each of the two protons will be in a different magnetic field as the result of the presence of the Fe^{2+} ions. In addition to the Zeeman interaction with the two different fields, the dipole-dipole interaction between protons on the same water molecule can lead to resolved structure in the line shape. The magnitude of any interaction between protons of different water molecules will be reduced by $1/r^3$, so that the effect will only be to broaden the line shapes. In addition, the line shapes appear to be affected by the presence of water molecules which we have called additional water, as they behave as though they are not part of the crystal structure.

4.1.1 Fine Structure of the Proton Lines

As the crystal contains ferromagnetic centres, it will be assumed that each proton is in a slightly different local field (c.f. [Bloembergen 1950], [Poulis 1951]). The source of the local fields will be discussed in Sec. 4.1.2. Assuming different local fields leads to the following line positions (in units of Gauss) and intensities:

$$\begin{array}{lll} & \textit{position} & \textit{intensity} \\ \left.\begin{array}{rcl} h &=& c+2a+\sqrt{a^2+b^2} \\ h &=& c-2a-\sqrt{a^2+b^2} \end{array}\right\} & & \dfrac{\left(-a+b-\sqrt{a^2+b^2}\right)^2}{a^2+b^2-b\sqrt{a^2+b^2}} \\ \left.\begin{array}{rcl} h &=& c+2a-\sqrt{a^2+b^2} \\ h &=& c-2a+\sqrt{a^2+b^2} \end{array}\right\} & & \dfrac{\left(-a+b+\sqrt{a^2+b^2}\right)^2}{a^2+b^2+b\sqrt{a^2+b^2}}, \end{array} \tag{4.1}$$

where

$$\begin{aligned} a &= \frac{1}{4}\frac{\gamma_H\hbar}{r^3}(1-3\cos^2\theta) \\ b &= \frac{1}{2}(H_1-H_2) \\ \text{and } c &= \frac{1}{2}(H_1+H_2). \end{aligned}$$

In these equations, γ_H is the gyromagnetic ratio of the protons, r is the separation of the protons, and θ is the angle between the proton-proton vector and the applied magnetic field. The direction of the applied magnetic field is considered to be the z direction. H_1 is the z component of the total magnetic field at one proton, and H_2 is the z component of the total magnetic field at the other.

A complete derivation of these equations parallels the work of Bloembergen very closely, and is given in Appendix C. The result gives a spectrum of two pairs of lines, where the two lines in each pair are of equal intensity.

Fig. 4.1 shows the relative positions and intensities for various ratios of $b:a$. The line patterns are each centred at c. As c is the average of the two local fields, it causes a shift in the centre of the system. This is not depicted in the figure because these shifts were not directly observable with our equipment, as we had no fixed reference signal to determine the absolute field of the observed line shapes. Note that for $b \ll a$, there are two lines separated by $6a$. These are the two lines which result from the

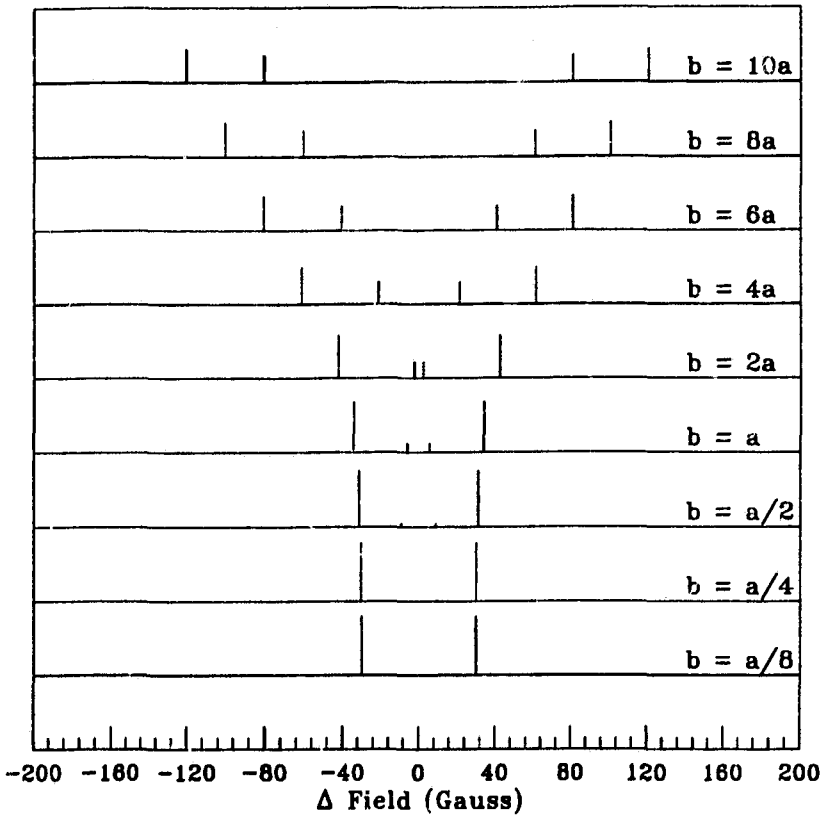

Figure 4.1: Line displacements for fixed a, and various choices of b. In this figure we have shifted the scale so that $c = 0$.

dipole-dipole interaction. When $b \gg a$ there are four lines which can be grouped into two pairs, one of which is at fields greater than c, and one of which is at fields less than c. The two lines in each pair are separated by $4a$, while the centres of the pairs are separated by $2b$. As a special case, if $a = 0$ we will see one line for $b \approx 0$ and two lines separated by $2b$ for $b > 0$.

We now have enough information about the line displacements to identify the orientations of the crystal with respect to the applied magnetic field, when the line displacements are compared to the relative positions of the peaks in the observed

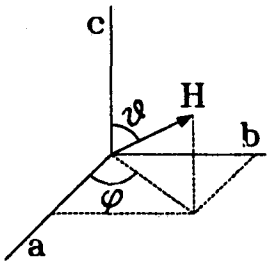

Figure 4.2: The spherical coordinate system.

data. For high temperatures it can be assumed that rapid thermal fluctuations of the local field inhomogeneities arising from the magnetic centres will tend to average these inhomogeneities to zero, leaving only the dipole-dipole interaction as a mechanism for creating fine structure in the lines of $CsFeCl_3 \cdot 2H_2O$. Using the coordinate system illustrated in Fig. 4.2, Fig. 4.3 shows the theoretical separations of the lines attributed to the dipole-dipole interactions of the eight pairs of protons in one unit cell of $CsFeCl_3 \cdot 2H_2O$. Eight separations were calculated and plotted. There are at most two non-equivalent dipole-dipole interactions, because of the symmetry of the crystal structure. Examination of Fig. 4.3 leads to the identification of the orientations of our crystal when compared with the line shapes plotted in Fig. 2.2.

We know that the observations were made with the applied field in a plane perpendicular to the b axis (i.e. $\phi = 0°$). In Fig. 4.3b, we note that at $\theta = 0°$ and $\theta = 180°$, all of the lines have the same small separations, so that if there is a reasonable amount of broadening, we expect to see only a single wide peak. At $\theta = 90°$ and $\theta = 270°$ all of the lines again have the same separations, but now the separation is large enough that we expect to see two distinct peaks in the line shape. At 27° on either side of each of $\theta = 90°$ and $\theta = 270°$, one of the pairs of lines is at maximum separation, while the other pair is at zero separation. In this case, we would expect to see three peaks, where the centre peak has twice the amplitude of the outer two

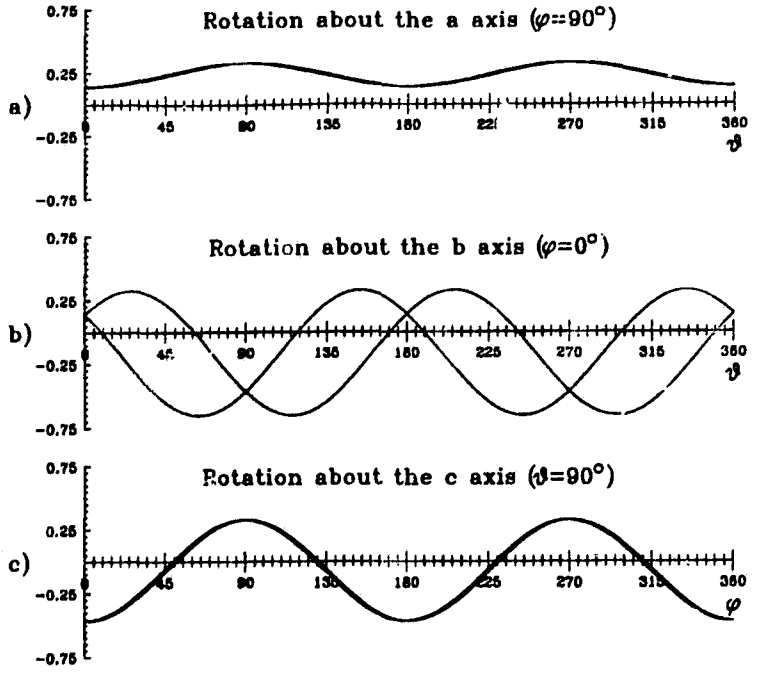

Figure 4.3: Line separations. This is only the result of the dipole-dipole interaction of all non-equivalent proton pairs. The separations are in arbitrary units.

peaks. Studying Fig. 2.2, we do indeed find this pattern. The single peaks occur at orientations of 80° and 260°, the double peaks occur at 170° and 350°, and the triple peaks occur about 30° on either side of these double peak orientations. Hence we have made the identification of the orientations of the crystal from the line shapes. Note that the asymmetry of the observed line shapes is not predicted by the interactions discussed to this point.

The main reasons for choosing the 0° and 90° orientations in the temperature dependant studies are also made clear in Fig. 4.3b. For the 0° orientation, we have only one unique separation of the lines attributed to the dipole-dipole interaction, and the lines should be close enough together to appear as one line if the broadening is

sufficient. This implies that any structure in the line shape should be attributed to the interaction of the protons with the magnetic centres only. At the 90° orientation, we again have only one separation of the lines attributed to the dipole-dipole interaction, but in this case, the two lines should be far enough apart not to appear as a single line. In this case we would expect to see four lines whose positions vary (as b varies) as in Fig. 4.1.

4.1.2 The Magnetic Interaction

Kopinga et al. [1985] use a Hamiltonian for the iron spin system given by

$$\mathcal{H}_{chain} = -J\sum_i \mathbf{S}_i\cdot\mathbf{S}_{i+1} + D\sum_i S_{iz}^2,$$

where $\mathbf{S}_i$ represents the full spin of the i_{th} iron nucleus. In this system, $S = 2$. In the case of $CsFeCl_3{\cdot}2H_2O$, Kopinga et al. find

$$\frac{J}{k} = -6.0 \pm 0.5 \text{ K}$$

$$\text{and } \frac{D}{k} = -40 \pm 20 \text{ K}.$$

By following the explanation in Sec. 1.1, we can see that this crystal is antiferromagnetic, with an easy axis of magnetization.

We need to add the Zeeman interaction of the iron spins with the applied magnetic field, $\mathbf{H}_0$, in order to have a complete Hamiltonian for the Fe^{2+} ions:

$$\mathcal{H}_z = -\sum_i \beta\mathbf{S}_i\cdot\mathbf{g}_i\cdot\mathbf{H}_0,$$

where β is the Bohr magneton, and $\mathbf{g}_i$ is the $\mathbf{g}$-tensor for the i^{th} spin. The total Hamiltonian for the Fe^{2+} ions is then

$$\begin{aligned}\mathcal{H} &= \mathcal{H}_z + \mathcal{H}_{chain} \\ &= -\sum_i \beta\mathbf{S}_i\cdot\mathbf{g}\cdot\mathbf{H}_0 - J\sum_i \mathbf{S}_i\cdot\mathbf{S}_{i+1} + D\sum_i S_{iz}^2. \qquad (4.2)\end{aligned}$$

In Appendix D, we show that $\overline{\mu}_k$, which is the time averaged magnetic moment of the k^{th} spin, is given in dyadic notation for terms up to $\mathcal{O}(T^{-2})$ by

$$\begin{aligned}\overline{\mu}_k &= \frac{\beta^2}{3kT}S(S+1)\mathbf{g}_k\cdot\mathbf{g}_k\cdot\mathbf{H}_0 \\ &\quad + \frac{\beta^2}{3k^2T^2}S(S+1)\mathbf{g}_k\cdot\left\{\frac{1}{3}S(S+1)\left(J\mathbf{g}_{k-1}+D\mathbf{g}_k+J\mathbf{g}_{k+1}\right)\right. \\ &\quad \left. - D\frac{1}{5}\left[\left(S(S+1)+\frac{1}{2}\right)(\hat{\imath}\hat{\imath}+\hat{\jmath}\hat{\jmath})+(3S(S+1)-1)\hat{\mathbf{k}}\hat{\mathbf{k}}\right]\cdot\mathbf{g}_k\right\}\cdot\mathbf{H}_0.\end{aligned}$$

We know S, J, and D for this system, and if we make the assumption that the **g**-tensors do not change with position within the crystal, then $\mathbf{g}_{k-1}=\mathbf{g}_k=\mathbf{g}_{k+1}=\mathbf{g}$, and we have that

$$\overline{\mu}_k = \frac{2\beta^2}{kT}\mathbf{g}\cdot\mathbf{g}\cdot\mathbf{H}_0+\frac{2\beta^2}{kT^2}\mathbf{g}\cdot\left\{-104\mathbf{g}+\left[52(\hat{\imath}\hat{\imath}+\hat{\jmath}\hat{\jmath})+122\hat{\mathbf{k}}\hat{\mathbf{k}}\right]\cdot\mathbf{g}\right\}\cdot\mathbf{H}_0.$$

Given a complete knowledge of **g**, we could predict values of $\overline{\mu}_k$ for any $\mathbf{H}_0$, but this is not possible, nor do we have enough data on $\overline{\mu}_k$ to calculate **g**.

One essential feature of the magnetic moment which follows from this equation is that the general dependance of the magnitude of the mean magnetic moment on temperature is of the form

$$\overline{\mu}_k = C_1\frac{1}{T}+C_2\frac{1}{T^2}. \tag{4.3}$$

If this magnetic moment theory is correct, we would expect to see such a temperature dependance of the local fields resulting from the iron spins.

If we study Fig. 3.1, we see that for the 0° orientation there is a definite increase in the separation of the peaks as the temperature decreases. We note that there is no evidence of a dipole-dipole line splitting, except perhaps in one peak of the 32 K line shape. The broadening of the peaks results in the dipole-dipole line pairs being unresolved, as we had hoped, and we can consider a in Eq. (4.1) to be effectively zero. This means that the peak to peak separation of the outer peaks will be equal

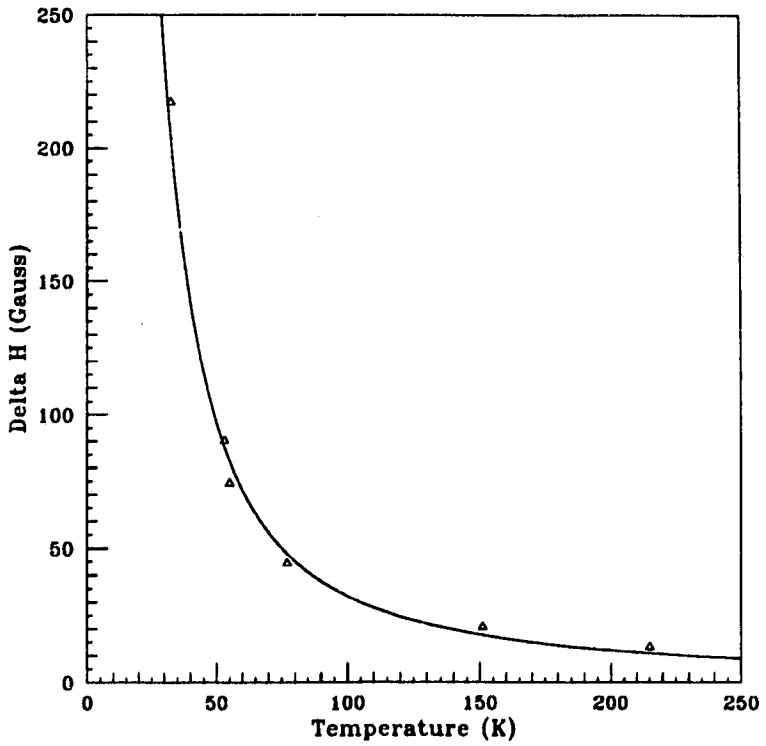

Figure 4.4: The temperature dependance of the line splitting. This is the 0° orientation.

to $2b$, which is the difference in the local fields at each proton site. The peak to peak separation of the outermost peaks was measured, and a quadratic in $1/T$ of the form Eq. (4.3) was fit to the measured data. The results are plotted in Fig. 4.4, and the values for C_1 and C_2 are given in Table 4.1. We note that the temperature dependance of the magnetic interaction behaves just as was expected.

For the 90° line shape (Fig. 3.3), on the other hand, we can see no temperature dependance of the line shape separations. This means that the temperature dependant magnetic interaction produces local fields which are the same at all of the proton sites at this orientation, and only the dipole-dipole interaction is producing the line splitting.

	Orientation	C_1	C_2	χ^2
Line splitting	0°	1573.822	163127.363	12.77
Line shift	0°	-1504.782	91563.055	3.809

Table 4.1: Fits to $C_1/T + C_2/T^2$ for the proton line splitting and the line shift. The χ^2 values are only for comparison of the two fits to each other.

For both orientations, we now have a theory which predicts the positions and amplitudes of the major components of the line shapes at two orientations for a range of temperatures. This theory does not predict line shapes with any asymmetry.

4.1.3 Line Broadening

Once the position of each peak has been determined, the line widths must be calculated in order to obtain a complete line shape. For $CsFeCl_3 \cdot 2H_2O$, there are three measurable contributions to the line widths:

1. The proton-proton dipolar interaction between protons which are not on the same water molecules. These contribute to the second moment of the j^{th} proton peak according to the equation

$$\langle \Delta H^2 \rangle = \frac{3}{4}\gamma_H^2 \hbar^2 I(I+1) \sum_k \left(\frac{1 - 3\cos^2 \theta_{jk}}{r_{jk}^3} \right)^2$$

   where r_{jk} is the inter-proton distance, and θ_{jk} is the angle between the inter-proton vector and the applied magnetic field [Abragam, 1961]. The sum over k was calculated for all protons within a radius of three of the smallest unit cell dimensions, excluding the one on the same water molecule.

2. The proton-cesium dipolar interaction. The actual values for this contribution range from one to ten percent of the proton-proton interaction, depending on

θ_{jk}. The contribution to the second moment of the j^{th} proton peak is given by

$$\langle \Delta H^2 \rangle = \frac{1}{3}\gamma_{Cs}^2 \hbar^2 S(S+1) \sum_k \left(\frac{1 - 3\cos^2 \theta_{jk}}{r_{jk}^3} \right)^2$$

where r_{jk} is the proton-cesium separation, and θ_{jk} is the angle between the proton-cesium vector and the applied magnetic field [Abragam, 1961]. The sum over k was calculated for all cesium nuclei within a radius of three of the smallest unit cell dimensions.

3. The proton-iron interaction. This interaction was not calculated theoretically. The broadening was observed experimentally as the residual broadening of the peaks after the first two contributions were subtracted. Table 4.2 contains these values.

   If we consider the third contribution to the broadening to be the result of a spread in the local magnetic field resulting from the iron spins as seen by each proton, we would expect this field, and hence its associated broadening, to have the same type of temperature dependance as given in Eq. (4.3). This temperature dependance can not be confirmed with the present data, as the numerical fit is inconclusive.

If we attempt to generate theoretical line shapes using the interactions described so far, we do not yet obtain a good fit to the observations. For the 0° orientation, where theory predicts only one symmetric peak at high temperatures and two equal amplitude symmetric peaks for lower temperatures, we observe one asymmetric peak at high temperatures and three peaks at low temperatures. As the outer peaks have equal amplitudes, we associate these with the peaks predicted by our theory. This leaves the asymmetry of the higher temperature peaks and the centre component of the lower temperature peaks to be explained.

For the 90° orientation, there is no temperature dependance of the peak separations, so it must be assumed that, for this orientation, the local iron fields are

θ	Temp. (K)	ΔH (Gauss)	Shift (Gauss)	Proton-iron Broadening (Gauss^2)	Additional Component Broadening (Gauss^2)	Additional Component Fraction
0°	32.5	217.58	33.3	150	33	0.31
0°	53	90.66	6.23	27	24.0	0.26
0°	55	74.62	3.10	17.5	23.8	0.29
0°	77	44.82	-2.5	7.8	23	0.19
0°	151	21.06	-9.0	4.5	15	0.31
0°	215	13.60	-4.7	7.0	15	0.31
90°	32	0.0	-5.0	30.0	20	0.45
90°	55	0.0	-7.5	10.0	7.0	0.19
90°	77	0.0	-7.2	7.2	7.0	0.11
90°	195	0.0	-7.0	3.6	2.1	0.14
90°	240	0.0	-6.7	2.8	1.8	0.13
90°	253	0.0	-6.3	2.5	3.0	0.10

Table 4.2: Parameters from model fit. θ is the orientation in the *ac* plane. ΔH is the difference in the magnetic field at each proton site as measured by the line splittings. The proton-iron broadening is the residual broadening of each of the components of the total line shapes. The additional component fraction is the ratio of the area of the additional component to the area of the total line shape. The values in the table were determined to an accuracy of about ± 1 in the last digit. These were the best values allowed by a visual fit to the observed line shapes.

the same, and the interaction is essentially a dipole-dipole interaction. The theory then predicts two symmetric peaks of equal amplitude. The observations give two peaks with unequal amplitudes, the greater amplitude one of which shows a definite asymmetry.

If we make an attempt to fit our theoretical line shapes to the observed line shapes at the 90° orientation, it is obvious that the predicted dipolar line splitting is twice the splitting of the observed lines. Agreement between theoretical and observed line shapes can be achieved by increasing the proton-proton separations calculated from the published structural data (Basten et al. [1978], Table 1.1) by a factor of 1.3 ± 0.1. This may reflect an error in the published nuclear positions, or may be the result of

additional motion of water molecules in the material.

We have assumed that the protons in our crystal would be located at the same sites as the deuterium nuclei in Basten et al.'s crystal. It is possible that this assumption is not entirely correct, and that the protons in our crystal are further apart than in the deuterated crystal. Another possibility which has been suggested is that neutron diffraction results from a hydrogenated crystal with additional water (such as ours) could give proton-proton separations which are smaller than the rigid lattice values indicated by the dipolar interaction. It is also possible that there was blurring of the neutron diffraction reflections due to a component similar to our additional water. In order to resolve the question of the proton-proton separations, it would be useful to perform a neutron diffraction analysis on the same crystal from which our CW NMR line shapes have been obtained.

Additional line shape work may also give some insight into the problem. It is interesting to note that although it is possible to obtain satisfactory model fits to the 0° orientation observations without the separation factor of 1.3, the agreement is better if the proton separations are increased. If the assumed positions are indeed in error, it follows that the factor of 1.3 should be used at all orientations. For this reason, all of the line shape results have been obtained under the assumption that the proton-proton separations predicted by Basten et al.'s values should be increased by 1.3.

At the 0° orientation, we fit our theoretical line shape so that one of the peaks matched the lower intensity peak of the observed line shape, and then subtracted the theoretical line shape from the observed line shape. The remaining signal was a single peak which was very similar in appearance to the unexplained portion of the 0° orientation line shapes. In the following section we present our explanation of the remainder of the line shapes at both orientations.

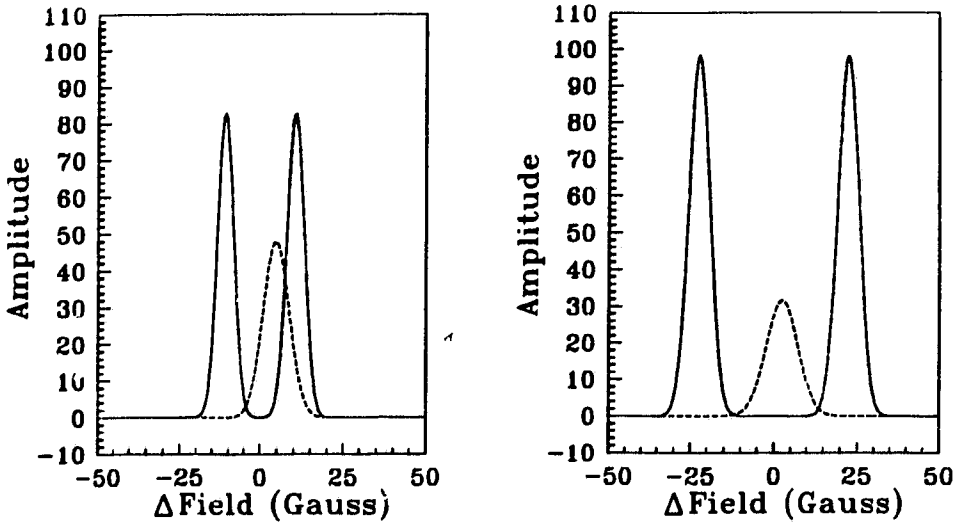

Figure 4.5: Two line shape components for the 0° orientation at two temperatures. The left line shape is for 151 K. The right line shape is for 77 K. The solid line is the line shape resulting from the fine structure, and the dashed line is the additional water line shape.

4.1.4 The Additional Water

Although the model described so far does appear to give a good fit to part of the data, there is still the problem of explaining the remainder of most of the line shapes, and the centre component of the 0° low temperature line shapes. As was stated at the beginning of Chap. 3, these components were not observed in the few preliminary line shapes obtained from a newly grown crystal.

The difference between the model and the observed line shapes can be explained by postulating that there are additional water molecules present in the crystal sample. If there are dislocations and impurities inside the crystal, it seems reasonable to suggest that there are water molecules present which are not part of the crystal structure, and are relatively free to reorient at random. Alternatively, water molecules could have been absorbed on the surface of the crystal. Both of these possibilities would produce a single line with its centre at the average magnetic field of the crystal.

As we see in Table 4.2, the ratio of the area of additional water component to

the area of the total line shape indicates that the additional water is ten to thirty percent of the water present in the crystal. This does not rule out unattached water molecules, but thirty percent is perhaps too large a proportion for included or absorbed unattached water. Also, the ratio appears to be orientation dependant, which also does not agree with the water molecules being unattached to the crystal. Another problem with the water being unattached is that the water would then be free to diffuse through the crystal, which would create a line width broader than that which was observed.

Another possibility is that the additional water component may be due to restricted motions of water molecules which are still part of the crystal structure, but are not held rigid because of a partial breakdown of the hydrogen bonding. This could cause the structure of the line shape contribution of these partially detached water molecules to collapse to a single line. The suggestion of easily broken bonds agrees with the fact that the crystal structure is destroyed when attempts are made to remove unattached water from the crystal (see Sec. 2.1).

An attempt was made to fit a Lorentzian line shape to the additional water component. This, however, gave a line shape which definitely did not agree with the observed shape. A better fit was obtained with a Gaussian line shape, although the observed lines did tend to be slightly wider in the wings. For the 0° orientation at two temperatures, Fig. 4.5 shows the line shape resulting from the fine structure calculations, as well as the line shape which fits the additional water component. The additional water line widths are given in Table 4.2.

If the additional water line is located at the average field of the crystal, then it should act as an unchanging position from which the shift of the crystal line shapes can be measured. This does appear to be the case, as the difference between the line pattern centres and the additional water line centre fits a temperature relation of the form Eq. (4.3). The parameters of this fit are given in Table 4.1.

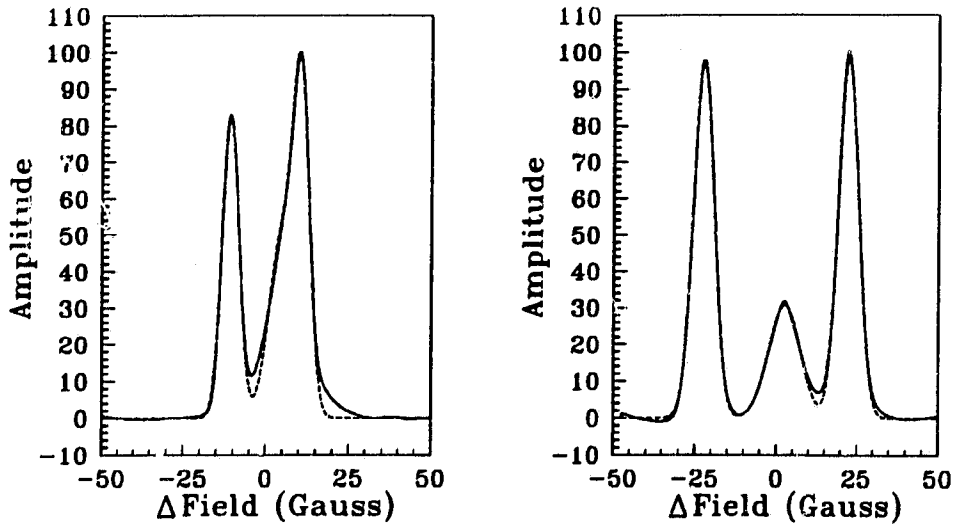

Figure 4.6: Two model fits for the 0° orientation. The left line shape is for 151 K. The right line shape is for 77 K. The solid line is the observed line shape, and the dashed line is the theoretical line shape, which is the sum of the fine structure line shape and the additional water line shape.

4.1.5 The Total Line Shapes

If we combine all the effects described to this point, we can produce theoretical line shapes which agree well for the 0° orientation and the 90° orientation. Fig. 4.6 and Fig. 4.7 show two representative fits for the two orientations.

The line shapes agree very well, except near the baseline. There are two possibilities which could account for this baseline problem. The first is that there may have been some problems with the baselines of the derivative line shapes drifting slightly during the scans. The second possibility is that the additional water line shape does not appear to be perfectly Gaussian, and the small extension of the wings of the line may be causing a slight increase in the amplitude of the observed line near the additional water line.

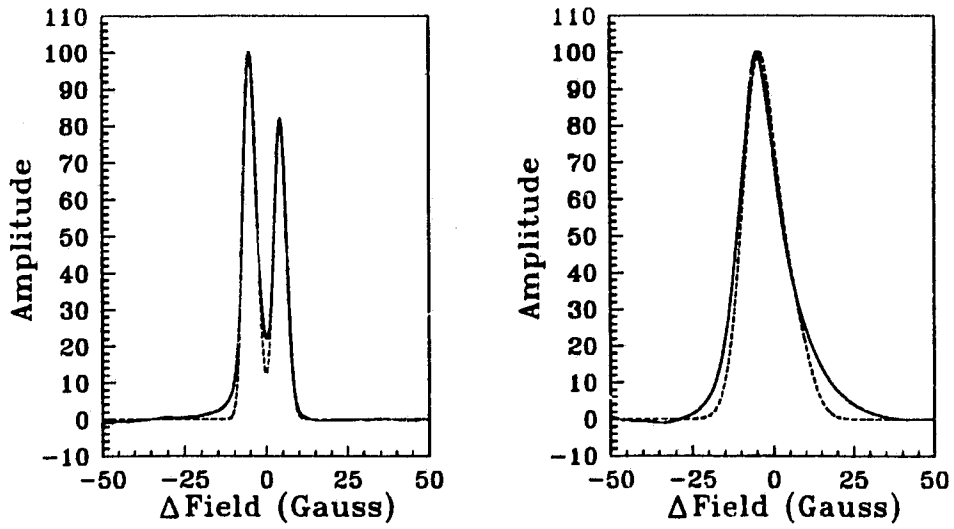

Figure 4.7: Two model fits for the 90° orientation. The left line shape is for 245 K. The right line shape is for 32 K. The solid line is the observed line shape, and the dashed line is the theoretical line shape.

4.2 The Spin Lattice Relaxation

4.2.1 Soliton Relaxation

In order to create a theoretical model for the nuclear spin-lattice relaxation, we will proceed in a manner similar to Abragam [1961]. Consider a Hamiltonian for the complete system:

$$\mathcal{H} = \mathcal{H}_o + \mathcal{F} + \mathcal{H}_1$$

where $\mathcal{H}_o$ is the unperturbed Hamiltonian of the proton spin system, $\mathcal{F}$ is the unperturbed Hamiltonian of the lattice composed of magnetic iron spins, and $\mathcal{H}_1$ is the coupling between the proton spins and the lattice.

To begin, we will not sum over each of the proton spins. In this case $\mathcal{H}_o$, $\mathcal{F}$, and $\mathcal{H}_1$ are given by

$$\mathcal{H}_0 = -\gamma \mathbf{I}\cdot\mathbf{H}_0$$

$$\begin{aligned}\mathcal{F} &= \frac{1}{\hbar}\left[-\beta\sum_k \mathbf{S}_k\cdot\,\mathbf{g}_k\cdot\mathbf{H}_0 - J\sum_k \mathbf{S}_k\cdot\mathbf{S}_{k+1} + D\sum_k S_{kz}^2\right]\\ \mathcal{H}_1 &= -\gamma\mathbf{I}\cdot\mathbf{H}_1\end{aligned}$$

where the terms in $\mathcal{F}$ are defined as in Eq. (4.2), $\mathbf{I}$ is the proton spin, and $\mathbf{H}_1$ is the local field resulting from the iron spins as seen by the proton.

We are interested in the relaxation, which is produced by the interaction between the spins and the lattice, so we will consider $\mathcal{H}_1$. This can be written in the form $\mathcal{H}_1 = \sum_q F^{(q)}A^{(q)}$, where $F^{(q)}$ are lattice operators, and $A^{(q)}$ are spin operators. If we evaluate $\mathcal{H}_1$, and use the definition of the raising and lowering nuclear spin operators, we find that

$$\mathcal{H}_1 = -\gamma\left[\left(\frac{H_{1x}-iH_{1y}}{2}\right)I^+ + \left(\frac{H_{1x}+H_{1y}}{2}\right)I^- + H_{1z}I_z\right],$$

and we can identify

$$\begin{aligned} F^{(0)} &= H_{1z} & A^{(0)} &= -\gamma I_z\\ F^{(1)} &= \tfrac{H_{1x}-iH_{1y}}{2} & A^{(1)} &= -\gamma I^+\\ F^{(-1)} &= \tfrac{H_{1x}+iH_{1y}}{2} & A^{(-1)} &= -\gamma I^-\end{aligned}$$

To find the relaxation time, we need to find an equation for the longitudinal magnetization of the form

$$\frac{d\langle I_z\rangle}{dt} = -(a_z - a_0),$$

where $a_z = Tr\{\mathcal{A}_z\sigma^*\} = \langle\mathcal{A}_z\rangle$ and

$$\mathcal{A}_z = \frac{1}{2}\sum_{q,p} J^{(q)}\left(\omega_p^{(q)}\right)\left[A_p^{(q)},\left[A_p^{(-q)},I_z\right]\right],$$

where $J^{(q)}\left(\omega_p^{(q)}\right)$ is the spectral density, and

$$A^{(q)}(t) = e^{i\mathcal{H}_0 t}A^{(q)}e^{-i\mathcal{H}_0 t} = \sum_p A_p^{(q)}e^{i\omega_p^{(q)}t}.$$

This gives

$$\begin{aligned} e^{i\mathcal{H}_0 t} A^{(0)} e^{-i\mathcal{H}_0 t} &= A^{(0)} \\ e^{i\mathcal{H}_0 t} A^{(1)} e^{-i\mathcal{H}_0 t} &= A^{(1)} e^{i\omega_I t} \end{aligned}$$

(ω_I is the resonance frequency of the protons) so that

$$\mathcal{A}_z = \frac{1}{2}\left(J^{(1)}(\omega_I)\left[A^{(1)},\left[A^{(-1)},I_z\right]\right] + J^{(-1)}(\omega_I)\left[A^{(-1)},\left[A^{(1)},I_z\right]\right]\right).$$

From the standard commutation relations, we can show that

$$\begin{aligned} \left[A^{(1)},\left[A^{(-1)},I_z\right]\right] &= \gamma^2\left[I^+,\left[I^-,I_z\right]\right] \\ &= 2\gamma^2 I_z \end{aligned}$$

and that

$$\left[A^{(-1)},\left[A^{(1)},I_z\right]\right] = 2\gamma^2 I_z$$

also. This means that

$$\mathcal{A}_z = 2\gamma^2 J^{(1)}(\omega_I) I_z$$

and

$$\begin{aligned} \frac{d\langle I_z\rangle}{dt} &= -2\gamma^2\left(\langle I_z\rangle - \langle I_z\rangle_0\right) J^{(1)}(\omega_I) \\ &= -\frac{1}{T_1}\left(\langle I_z\rangle - \langle I_z\rangle_0\right) \end{aligned}$$

where

$$\frac{1}{T_1} = 2\gamma^2 J^{(1)}(\omega_I)$$

Since the spin lattice coupling Hamiltonian is accounted for, we will write $J^{(1)}(\omega_I)$ as $J(\omega)$. In order to find a value for the spectral density $J(\omega)$, we use the fact that $J(\omega)$ is the Fourier transform of the correlation function $G(\tau)$. i.e.

$$\therefore \quad J(\omega) = \int_{-\infty}^{+\infty} G(\tau) e^{-i\omega\tau} d\tau$$

where

$$G(\tau) = \overline{H(\tau)H(0)} - \overline{H}^2 = G(-\tau),$$

a bar over a function denoting the ensemble average of the function. This is as far as we can proceed with general theory. In order to continue, we need a model for the mechanism which causes the spin-lattice relaxation. This will result in an expression for $G(\tau)$. Since there has been some success in using various soliton models to describe one dimensional antiferromagnetic systems (Goto and Yamaguchi [1981], Mikeska [1980], Tinus et al. [1982]), we have developed a statistical model for $G(\tau)$ based on the behavior of solitons. It was assumed that the solitons were all π kink solitons, and that the solitons had a width which was negligible when compared to the soliton separations, so that soliton interactions would not have to be considered. For π kinks, both solitons and antisolitons will have the same effect on an iron spin; the spin will flip by π radians. For an antiferromagnetic system, this means that at some point, the local field resulting from a chain of spins will be inverted whenever a soliton or an antisoliton passes that point.

Because the field has a constant magnitude with a direction which reverses for each passage of a soliton, we will only need to consider the probability of the net local field pointing up or down after the passage of a soliton. We will assume that the solitons are randomly distributed along the chain, so that the two orientations of the field occur with equal probability. First, we can see immediately that $\overline{H} = 0$, so that $G(\tau) = \overline{H(\tau)H(0)}$. If we call the local values of the field h and $-h$, we can write an equation for $\overline{H(\tau)H(0)}$:

$$\begin{aligned}\overline{H(\tau)H(0)} \;=\; & h^2 P[H(\tau) = h, H(0) = h] - h^2 P[H(\tau) = -h, H(0) = h] \\ & -h^2 P[H(\tau) = h, H(0) = -h] + h^2 P[H(\tau) = -h, H(0) = -h],\end{aligned}$$

where $P[H(\tau) = h, H(0) = h]$ is the probability that the field is h at time $t = \tau$ and

h at time $t = 0$. The other three probabilities have similar meanings. We can write

$$\begin{aligned}\overline{H(\tau)H(0)} &= h^2 P[H(\tau) = h|\ H(0) = h]\, P[H(0) = h] \\ &\quad -h^2 P[H(\tau) = h|\ H(0) = -h]\, P[H(0) = -h] \\ &\quad -h^2 P[H(\tau) = -h|\ H(0) = h]\, P[H(0) = h] \\ &\quad +h^2 P[H(\tau) = -h|\ H(0) = -h]\, P[H(0) = -h]\end{aligned}$$

where $P[H(\tau) = h|\ H(0) = h]$ is the conditional probability that the field is h at $t = \tau$ given that the field was h at $t = 0$.

The probability that the field at $t = \tau$ is the same as the field at $t = 0$ is the probability that an even number of solitons has passed during the interval τ. If we assume that the arrival of a soliton is a random event, and that the probability of the arrival of a soliton in some time interval does not depend on what has happened before the time interval, then we have an exponential distribution for the arrival times of the solitons, and the probability of n solitons passing a point in a time interval τ is given by the Poisson distribution

$$f(n) = \frac{(\lambda\tau)^n e^{-\lambda\tau}}{n!}, n = 0, 1, 2, \ldots$$

where λ is the arrival frequency of solitons passing any arbitrarily chosen point. The probability that the field at $t = \tau$ is the same as the field at $t = 0$ is given by

$$\begin{aligned}P[n \text{ even}] &= f(0) + f(2) + f(4) + \ldots \\ &= e^{-\lambda t} + \frac{(\lambda\tau)^2 e^{-\lambda\tau}}{2!} + \frac{(\lambda\tau)^4 e^{-\lambda\tau}}{4!} + \ldots \\ &= e^{-\lambda t}\left(1 + \frac{(\lambda\tau)^2}{2!} + \frac{(\lambda\tau)^4}{4!} + \ldots\right) \\ &= \frac{1}{2}\left(1 + e^{-2\lambda\tau}\right)\end{aligned}$$

The probability that the field at $t = \tau$ is different from the field at $t = 0$ is the

probability that the number of solitons passing a point in the interval τ is odd.

$$\begin{aligned} P[n \text{ odd}] &= 1 - P[n \text{ even}] \\ &= \frac{1}{2}\left(1 - e^{-2\lambda\tau}\right) \end{aligned}$$

Combining this with $P[H(\tau) = h] = \frac{1}{2}$, we can find an expression for $G(\tau)$:

$$\begin{aligned} G(\tau) &= \overline{H(\tau)H(0)} \\ &= h^2\frac{1}{2}\left(1 + e^{-2\lambda\tau}\right) - h^2\frac{1}{2}\left(1 - e^{-2\lambda\tau}\right) \\ &= h^2 e^{-2\lambda\tau},\ \tau > 0 \end{aligned}$$

This leads to an expression for $J(\omega)$:

$$\begin{aligned} J(\omega) &= \int_{-\infty}^{+\infty} G(\tau)e^{-i\omega\tau}d\tau \\ &= \int_{-\infty}^{0} G(\tau)e^{-i\omega\tau}d\tau + \int_{0}^{+\infty} G(\tau)e^{-i\omega\tau}d\tau \\ &= \int_{0}^{+\infty} G(-\tau)e^{i\omega\tau}d\tau + \int_{0}^{+\infty} G(\tau)e^{-i\omega\tau}d\tau \\ &= h^2\int_{0}^{+\infty} e^{(-2\lambda+i\omega)\tau}d\tau + h^2\int_{0}^{+\infty} e^{(-2\lambda-i\omega)\tau}d\tau \\ &= \frac{h^2}{-2\lambda+i\omega}\left[e^{(-2\lambda+i\omega)\tau}\right]_0^{+\infty} + \frac{h^2}{-2\lambda-i\omega}\left[e^{(-2\lambda-i\omega)\tau}\right]_0^{+\infty} \\ &= \frac{4\lambda h^2}{4\lambda^2+\omega^2} \end{aligned}$$

Which gives

$$T_1^{-1} = 2\gamma^2 h^2 \frac{4\lambda}{4\lambda^2+\omega^2}, \tag{4.4}$$

which will be the spin-lattice relaxation rate for one proton. We will need to find values for two quantities, namely λ and h, if we wish to calculate values for T_1^{-1}.

4.2.2 The Arrival Frequency of The Solitons

In order to consider the effect of solitons on the spin-lattice relaxation time, we need to have a model which describes the behavior of the magnetic spins under the influence of solitons. Mikeska [1980] has shown that for an antiferromagnetic system with a Hamiltonian of the form Eq. (4.2), the Hamiltonian can be transformed into a sine-Gordon equation, given the following assumptions:

- that the classical orientation of the spins changes slowly with position along the chain, so that we can make a continuum approximation for the spin orientations. This is equivalent to a low temperature approximation.
- that the applied magnetic field is small:

$$\frac{g\mu B}{JS} \ll 1.$$

In order to find the arrival frequency, λ, of the solitons, we use the fact that λ can be written as $\lambda = n_s u_s$, where n_s is the number density of the solitons and u_s is their mean speed. If we use the expressions from Tinus et al. [1982] for Mikeska's quantities, then

$$n_s = 8m\sqrt{\frac{\beta m}{\pi}}e^{-8\beta m}$$

$$u_s = \frac{2JS}{\hbar\sqrt{4\beta m}}$$

where

$$m = \sqrt{\frac{2D}{J}}$$

$$\beta = \frac{JS^2}{4kT}$$

(In these equations, the unit of length is the separation between the spins along the chain.) This value of n_s is twice that given by Tinus et al. because we must count the antisolitons as well as the solitons. Some simple algebra leads to

$$\lambda = \frac{4}{\hbar}\sqrt{\frac{2DJ}{\pi}}Se^{-8\beta m}. \tag{4.5}$$

If we combine this result with Eq. (4.4), and define $E_0 = 2S^2\sqrt{2DJ}$ as in Tinus et al., we obtain the same results as their coherent soliton model, namely

$$\begin{aligned} T_1^{-1} &\sim \tfrac{1}{\lambda} \sim \exp\left(\tfrac{E_0}{kT}\right) \quad \text{for } \omega \ll \lambda \\ T_1^{-1} &\sim \lambda \sim \exp\left(-\tfrac{E_0}{kT}\right) \quad \text{for } \omega \gg \lambda. \end{aligned}$$

4.2.3 The Fluctuating Local Field

We can find a value for the local field, h, attributed to the antiferromagnetic chains in the following manner. The coupling between inter-chain spins is at least two orders of magnitude less than the coupling between intra-chain spins [Smeets et al., 1985]. Hence we can assume that the spin lattice relaxation contribution of each chain is independant of all other chains.

At each proton site, the local field contribution from each chain was calculated by finding the vector sum of the fields at the proton site from each iron spin using the formula

$$\mathbf{H}_{local} = -\frac{\boldsymbol{\mu}_{Fe}}{r^3} + \frac{3(\boldsymbol{\mu}_{Fe}\cdot\mathbf{r})\mathbf{r}}{r^5}$$

where $\mathbf{r}$ is the position vector from the iron nucleus to the proton site, and $\boldsymbol{\mu}_{Fe}$ is the magnetic moment of the iron nucleus. The value of h^2 at the proton site is given by

$$h^2 = \left|\sum \mathbf{H}_{local}\right|^2.$$

Since the only part of Eq. (4.4) which changes from chain to chain is h^2, we can add the square of the local field contribution of each chain to find an effective h^2 at each

proton site. These calculations lead to values for the local field at the proton sites which agree with Basten et al. [1978].

Because of the symmetry of the crystal, each proton site in the unit cell could have a different effective h^2, which would lead to a different T_1^{-1} for each proton. If we assume that the protons have a common spin temperature, however, we can predict a macroscopic T_1^{-1} by averaging the values of T_1^{-1} from each proton. Mathematically, this is the same as averaging the squares of the local fields and calculating an overall effective h^2. The field resulting from this analysis was used to calculate the curve of T_1^{-1} as a function of temperature, which is shown in Fig. 3.4 and Fig. 3.5. As the theoretical predictions use no free parameters from the NMR results themselves, this agreement is strong evidence for the validity of the soliton relaxation model in this material. We note, however, that the range in T_1^{-1} at each temperature is not accounted for in this model.

The model assumed that there was thermal motion of the iron spins which caused them to rotate about the a axis. This would cause the contribution of each iron spin to the local magnetic field to be reduced to $\mathbf{H}_{local} \cos \phi_m$, where ϕ_m is the canting angle.

Both the 0° and 90° orientations appear to be well fitted by the stochastic soliton model insofar as the temperature dependance is concerned. However, the stochastic soliton model does not predict the range of T_1^{-1} values at a given temperature. If the assumption that the protons all have a common spin temperature is not completely valid, then we may have two or more values for T_1^{-1}. For the 0° orientation, where the local fields can be quite different, this could result in two spin temperatures. As we move across the signal response range, we would measure "mean" values for T_1^{-1} which would be anywhere between the two actual values. At high temperatures, where the line shape is a single peak, we would expect the proton systems to have nearly the same spin temperature, and the variation in T_1^{-1} would be small. For lower temperatures, where the line shape results from larger differences in the local fields,

we would measure larger variations in T_1^{-1}. This is the type of behavior we see in the data in Fig. 3.4.

4.2.4 The Magnon Model

The alternative model to predict the spin-lattice relaxation (T_1) of $CsFeCl_3 \cdot 2H_2O$ is the three magnon process. Goto and Yamaguchi [1981] find that this is a good fit to the high field ($H > 7$ kG) relaxation times for $CsNiF_3$. In this model, T_1^{-1} is given by

$$T_1^{-1} \sim T^2 e^{-2\varepsilon_{AE}/kT},$$

where ε_{AE} is the gap energy given by (β is the Bohr magneton.):

$$\varepsilon_{AE} = \sqrt{g\beta H(2DS + g\beta H)}.$$

If we examine the equation for the relaxation time, we immediately see that we have a function which increases as the temperature increases. This is the inverse of the temperature dependance of the data as well as the soliton model, and we must conclude that the three-magnon process is not a valid model for proton spin-lattice relaxation in $CsFeCl_3 \cdot 2H_2O$.

4.3 Chapter Summary

- The positions of the peaks of the proton line shapes are due to the interaction of two protons in slightly different magnetic fields. Agreement between the theoretical and observed line shapes was achieved by increasing the proton-proton separations by a factor of 1.3±0.1.
- The temperature dependance of the local fields is of the form

$$\overline{\mu}_k = C_1 \frac{1}{T} + C_2 \frac{1}{T^2}.$$

- Line broadening is due to dipolar interactions of protons with other protons, cesium nuclei, and iron nuclei.

- There is a component of the line shapes which is explained by the presence of water molecules which are not part of the crystal structure, and which are free to reorient at random.

- The spin-lattice relaxation can be explained by a simple stochastic theory which treats magnetic disturbances in the lattice as solitons moving along chains of Fe^{2+} ions. The spin-lattice relaxation rate is given by the expression

$$T_1^{-1} = 2\gamma^2 h^2 \frac{4\lambda}{4\lambda^2 + \omega^2},$$

  where λ is given by

$$\lambda = \frac{4}{\hbar}\sqrt{\frac{2DJ}{\pi}} S e^{-8\beta m}.$$

- The three-magnon model does not agree with the data.

Chapter 5

Conclusions

5.1 The Line Shapes

For magnetic fields applied along the a or c axes, our model gives good agreement with the observed line shapes, over a large range of temperatures. In this model, the two protons on the same water molecule are not considered to be in the same magnetic field. Instead, the local fields are considered to be affected by the magnetic moments of the iron spins. When the differing local fields are combined with the proton dipole-dipole interaction, the resulting line positions produce symmetric patterns of up to four peaks for each proton pair. The local fields have the same temperature dependance as the mean magnetic moments of the iron spins, namely

$$\overline{\mu}_k = C_1 \frac{1}{T} + C_2 \frac{1}{T^2}.$$

This model explains the major portion of the observed line shapes if we increase the proton-proton separation by a factor of 1.3±0.1. Further line shape studies may lead to the resolution of this discrepancy, but a neutron diffraction study of a $CsFeCl_3 \cdot 2H_2O$ crystal which contains the additional water component may be necessary to completely resolve the problem.

The remainder of the line shapes does not behave as though it results from protons which are part of the crystal structure. Instead, there are water molecules, which have

been called additional water, which are free to reorient in such a manner that their contribution to the line shape is a single symmetric peak which is nearly Gaussian in shape.

The symmetric line shape from the dipole-dipole interaction is centred on the average magnetic field in the crystal. The symmetric additional water line, on the other hand, appears to be centred on the applied magnetic field. The resulting line shape, which is the sum of the two contributions, is an asymmetric line shape which agrees well with the observed line shapes.

For fields applied in directions other than along the a or c axes, the theory is not yet successful, because of a lack of information about the **g**-tensor. A low temperature study of the line shapes at a large number of different orientations would allow the line shapes to be modelled more easily and more accurately than a similar study at (or near) room temperature. The low temperature line shapes would have larger separations of the peaks, which would make various features easier to identify and measure. Such a study, combined with the theory which has been developed, should give enough information to allow the **g**-tensor to be calculated.

The problem of the additional water contamination of the crystal could be addressed in two ways. The first is that a new crystal could be grown. If measurements are obtained immediately, there may not be any significant additional water component to the line shapes. The second method would be to grow a deuterated crystal (i.e. $CsFeCl_3 \cdot 2D_2O$) and perform nuclear quadrupole resonance (NQR) experiments on this crystal. The NQR results should locate the additional nuclei in the crystal structure. Also, the results would indicate the source of the additional nuclei. If the additional nuclei are being absorbed from the environment in which the crystal is stored, then the deuterated crystal would have an additional component which arises from protons. On the other hand, if the additional nuclei are the result of the waters of hydration breaking their bonds with the crystal, then the additional component would result from the deuterium.

5.2 The Spin-Lattice Relaxation

We can treat the π-kink solitons as non-interacting infinitesimal particles travelling along the chains of iron spins. This treatment leads to an arrival time problem which can be analyzed stochastically to give an accurate prediction of the temperature dependance of the spin-lattice relaxation. The relaxation rate is given by

$$T_1^{-1} = 2\gamma^2\hbar^2 \frac{4\lambda}{4\lambda^2 + \omega^2},$$

where λ is the soliton arrival frequency, given by

$$\lambda = \frac{4}{\hbar}\sqrt{\frac{2DJ}{\pi}} S e^{-8\beta m}.$$

The three-magnon model leads to a different expression for the temperature dependance of the relaxation rate which does not agree with either the stochastic theory, or the observations, which leads us to conclude that this mechanism plays no significant role in the proton relaxation.

While the stochastic soliton model predicts the temperature dependance of the relaxation times, it does not predict the range of T_1 values at a given temperature. Further investigation of the common spin temperature assumption is necessary, since the range of T_1 values is probably the result of two (or more) systems with different spin temperatures. Some preliminary work has been done which indicates that the structure of the FID is related to differing T_1 components. With new data analysis procedures, and an improved spectrometer, it may be possible to analyse the FID to find different relaxation times, something which can not yet be done with our equipment.

In order to predict the full range of T_1 values with the current model, the internal fields must vary by fifty percent of the field predicted using the method described in Section 4.2.3. There is some evidence that this is possible, but a more detailed

knowledge of the behavior and orientations of the magnetic centres within the crystal will be needed before any conclusions can be made.

References

Abragam, A. 1961. *Principles of Nuclear Magnetism.* Oxford University Press, Oxford.

Basten, J.A.J., van Vlimmeren, Q. A. G., and de Jonge, W. J. M. 1978. Crystallographic and magnetic structure of $RbFeCl_3 \cdot 2H_2O$ and $CsFeCl_3 \cdot 2H_2O$. *Phys. Rev B.*, **18**, 2179-2184.

Bloembergen, N. 1950. Fine structure of the magnetic resonance line of protons in $CuSO_4 \cdot 5H_2O$. *Physica*, **XVI**, no.2, 95-112.

Drazin, P.G. 1983. *Solitons, London Mathematical Society Lecture Note Series.* Cambridge University Press.

Efron, B. 1982. *The Jackknife, the Bootstrap and Other Resampling Plans.* CBMS-NSF Regional Conference Series in Applied Mathematics Monograph 38. Society for Industrial and Applied Mathematics, Philadelphia.

Goto, T. and Yamaguchi, Y. 1981. Effect of Magnetic Soliton on ^{133}Cs Nuclear Spin-Lattice Relaxation in $CsFeF_3$. *J. Phys. Soc. Japan*, **50**, no.7, 2133-2134.

Kopinga, K., Steiner, M., and de Jonge W.J.M. 1985. Quasi-one-dimensional magnetic behavior of the Ising system $CsFeCl_3 \cdot 2aq$. *J. Phys. C: Solid State Phys.*, **18**, 3511-3520.

Le Fever, H.Th., Thiel, R.C., Huiskamp, W.J., and de Jonge, W.J.M. 1981a. Crystal field effects in the compounds $RbFeCl_3 \cdot 2H_2O$ and $CsFeCl_3 \cdot 2H_2O$. *Physica*, **111B**, 190-208.

Le Fever, H.Th., Thiel, R.C., Huiskamp, W.J., de Jonge, W.J.M., and van der Kraan, A.M. 1981b. Magnetic ordering in the compounds $RbFeCl_3 \cdot 2H_2O$ and $CsFeCl_3 \cdot 2H_2O$. *Physica*, **111B**, 209-218.

Mikeska, H.J. 1980. Non-linear dynamics of classical one-dimensional antiferromagnets. *J. Phys. C: Solid State Phys.*, **13**, 2913-2923.

Nijhof, E.J., Gerritsma, G.J., and Flokstra, J. 1983. Temperature dependence of spin-cluster resonance intensity in $RbFeCl_3 \cdot 2H_2O$. *Physica*, **122B**, 333-337.

Poulis, N.J. 1951. Decomposition of the proton magnetic resonance line in paramagnetic crystals. *Physica*, **XVII**, 392-404.

Scott Russell, J. 1844. Report on Waves. *Reports to the 14th Meeting of the British Association for the Advancement of Science*, 311-390.

Smeets, J.P.M. Frikkee, E., de Jonge, W.J.M. and Kopinga, K. 1985. Magnetic ordering processes in the quasi-one-dimensional metamagnets $RbFeCl_3 \cdot 2aq$ and $CsFeCl_3 \cdot 2aq$ (aq = H_2O, D_2O). *Phys. Rev. B*, **31**, 7323-7334.

Tinus, A.M.C., Denissen, C.J.M., Nishihara, H., and de Jonge, W.J.M. 1982. Nuclear relaxation in $CsFeCl_3 \cdot 2H_2O$ and $RbFeCl_3 \cdot 2H_2O$: influence of diffusive solitons. *J. Phys. C: Solid State Phys.*, **15**, L791-L796.

van Vlimmeren, Q.A.G. and de Jonge, W.J.M. 1979. Spin-cluster resonance in the pseudo-one-dimensional canted Ising antiferromagnet $RbFeCl_3 \cdot 2H_2O$. *Phys. Rev. B*, **19**, 1503-1514.

van Vlimmeren, Q.A.G., Swüste, C.H.W., de Jonge, W.J.M., van der Steeg, M.J.H., Stoelinga, J.H.M., and Wyder, P. 1980. Spin-cluster excitations in $RbFeCl_3 \cdot 2H_2O$. *Phys. Rev. B*, **21**, 3005-3014.

Appendix A

The Programmable Pulse Sequencer

The pulses output by the Spin-Lock Pulse Spectrometer can be triggered by digital logic level pulses. Collaboration and discussion with the University of Victoria Department of Physics and Astronomy Electronics Shop resulted in the design and construction of a circuit which plugs into the backplane of an IBM-PC-XT type of computer and triggers the spectrometer pulses. We have called this circuit the Programmable Pulse Sequencer (PPS).

The circuit is based on three Intel 8254 Programmable Interval Timers controlled through a JDR Microdevices PR2 PC-XT interface board. There are three outputs which are connected by cables to the three inputs on the spectrometer. This gives complete control over all of the spectrometer's pulse timing.

A complete description of the PPS is given in the manual written by the Electronics Shop. The mode used to create the $\frac{\pi}{2}$-τ-$\frac{\pi}{2}$ pulse sequences used in this work is known as the two pulse mode. In this mode the PPS is programmed so that when it receives a trigger signal from the software, one pulse is output on the A channel followed τ seconds later by one pulse on the B channel. This sequence is repeated

automatically at some programmed interval much greater than τ (and T_1) until the PPS is turned off by the computer. The possible range of values for τ is 10 μs up to 65535 s (about 18.2 hr). A number of other pulse sequences such as pulse saturation and spin locking are possible, but were not used in this research.

There was one feature of the PPS which proved useful in an application for which the PPS was not originally designed. The A output can be programmed to give a continuous sequence of regularly spaced pulses at programmable intervals. This proved to be invaluable as an external clock for the Tektronix 2230 Digitizing Oscilloscope. Using the PPS, we were able to clock the oscilloscope acquisition rate so that the time for one sweep was equal to the time for one scan of the CW magnetic field.

Appendix B

The Jackknife Method

In order to estimate the variance of various parameters, we have used a data resampling scheme called the jackknife. This appendix is simply a brief description of the jackknife method as explained by Efron [1982].

We describe the data set as an independant and identically distributed (i.i.d.) sample of size n drawn from an unknown probability distribution F on the real line,

$$X_1, X_2, \ldots, X_n \overset{\text{iid}}{\sim} F.$$

Let E_F indicate the expectation of some estimator with this data set, and let $\hat{\theta} = \hat{\theta}(X_1, X_2, \ldots, X_n)$ be the estimator. Then the variance of $\hat{\theta}$ is given by

$$\text{Var} = E_F \left[\hat{\theta}(X_1, X_2, \ldots, X_n) - E_F \hat{\theta} \right]^2.$$

The jackknife estimate of the variance is calculated by deleting one data point from the set, calculating a "deleted estimator", then replacing the data point. This is repeated for each of the n data points, and an estimate of the variance is then calculated in the following manner.

Let $\hat{\theta}_{(i)} = \hat{\theta}(X_1, X_2, \ldots, X_{i-1}, X_{i+1}, \ldots, X_n)$ denote the deleted estimator, and

let $\hat{\theta}_{(\cdot)} = \sum_{i=1}^{n} \hat{\theta}_i / n$. Then the formula for calculating the jackknife estimate of the variance is

$$\widehat{\mathrm{VAR}} = \frac{n-1}{n} \sum_{i=1}^{n} \left[\hat{\theta}_{(i)} - \hat{\theta}_{(\cdot)} \right]^2 ,$$

and the jackknife estimate of the standard deviation is simply

$$\mathrm{SD} = \sqrt{\widehat{\mathrm{VAR}}}.$$

The advantage of this method is that the only requirement on the sample distribution is that the data be drawn from independant and identical probability distributions.

This estimation is expected to be useful, since it slightly overestimates the variance and standard deviation. A brief Monte Carlo simulation on the functions we were fitting showed that this was indeed the case.

Appendix C

Fine structure of the proton line shapes

In order to derive Eqs. (4.1), we will follow Bloembergen's [1950] work quite closely. The definitions of a, b, and c used here differ from those of Bloembergen. If an attempt is made to compare the final results of the two derivations, they are identical except for some of the signs of the coefficients. These do not affect the line positions or the relative intensities, which are self consistent for both derivations, and produce the same results.

We want to consider the line shape produced by the interaction of two protons, where each proton is in a different local field. We will call the local fields $\mathbf{H}_1$ and $\mathbf{H}_2$, and we will assume that they are both oriented along the same direction. Call this direction the z direction. The Hamiltonian for the two proton system can be considered to have two parts:

$$\mathcal{H} = \mathcal{H}_{Zeeman} + \mathcal{H}_{dipolar},$$

where

$$\mathcal{H}_{Zeeman} = -\gamma\hbar(H_1 I_{1z} + H_2 I_{1z})$$

is the Zeeman interaction of each proton with its local field, and

$$\mathcal{H}_{dipolar} = \frac{-\gamma^2\hbar^2}{r^3}[\mathbf{I_1}\cdot\mathbf{I_2} - 3(\mathbf{I_1}\cdot\mathbf{n})(\mathbf{I_2}\cdot\mathbf{n})]$$

is the dipolar interaction between the two protons. r is the proton-proton separation, and θ is angle between the proton-proton vector and the applied magnetic field.If we assume that the Zeeman interaction dominates, we can make the secular approximation

$$\mathcal{H}_{dipolar} \approx \mathcal{H}_d = \frac{\gamma^2\hbar^2}{r^3}\left[\frac{3}{2}(1-3\cos^2\theta)I_{1z}I_{2z} - \frac{1}{2}(1-3\cos^2\theta)\mathbf{I_1}\cdot\mathbf{I_2}\right],$$

which means that

$$\mathcal{H} \approx -\gamma\hbar(H_1I_{1z} + H_2I_{2z}) + \frac{\gamma^2\hbar^2}{2r^3}(1-3\cos^2\theta)(3I_{1z}I_{2z} - \mathbf{I_1}\cdot\mathbf{I_2}). \qquad \text{(C.1)}$$

We wish to find the frequencies and intensities which result from this Hamiltonian. We know that $\mathbf{I_1}\cdot\mathbf{I_2} = I_{1x}I_{2x} + I_{1y}I_{2y} + I_{1z}I_{2z}$ by definition, so Eq. (C.1) becomes

$$\mathcal{H} \approx -\gamma\hbar(H_1I_{1z} + H_2I_{2z}) + \frac{\gamma^2\hbar^2}{2r^3}(1-3\cos^2\theta)(2I_{1z}I_{2z} - I_{1x}I_{2x} - I_{1y}I_{2y}).$$

Also, we have the identities $I_x = \frac{1}{2}(I^+ + I^-)$ and $I_y = \frac{1}{2i}(I^+ - I^-)$, so that

$$I_{1x}I_{2x} = \frac{1}{4}(I_1^+ + I_1^-)(I_2^+ + I_2^-) = \frac{1}{4}(I_1^+I_2^+ + I_1^-I_2^+ + I_1^+I_2^- + I_1^-I_2^-)$$

$$\text{and } I_{1y}I_{2y} = -\frac{1}{4}(I_1^+ - I_1^-)(I_2^+ - I_2^-) = -\frac{1}{4}(I_1^+I_2^+ - I_1^-I_2^+ - I_1^+I_2^- + I_1^-I_2^-),$$

which results in

$$I_{1x}I_{2x} + I_{1y}I_{2y} = \frac{1}{2}(I_1^-I_2^+ + I_1^+I_2^-).$$

This gives

$$\mathcal{H} \approx -\gamma\hbar(H_1I_{1z} + H_2I_{2z}) + \frac{\gamma^2\hbar^2}{2r^3}(1-3\cos^2\theta)\left(2I_{1z}I_{2z} - \frac{1}{2}I_1^+I_2^- - \frac{1}{2}I_1^-I_2^+\right). \qquad \text{(C.2)}$$

Since we are interested in pairs of protons, $|++\rangle$, $|+-\rangle$, $|-+\rangle$, and $|--\rangle$ are basis states of $\mathcal{H}$. The Hamiltonian acts on these states as follows :

$$\begin{aligned}
\mathcal{H}|++\rangle &= [-\alpha(H_1+H_2)+\alpha^2\beta]|++\rangle \\
\mathcal{H}|+-\rangle &= [-\alpha(H_1-H_2)-\alpha^2\beta]|+-\rangle - \alpha^2\beta|-+\rangle \\
\mathcal{H}|-+\rangle &= [\alpha(H_1-H_2)-\alpha^2\beta]|-+\rangle - \alpha^2\beta|+-\rangle \\
\mathcal{H}|--\rangle &= [\alpha(H_1+H_2)+\alpha^2\beta]|--\rangle,
\end{aligned}$$

where $\alpha = \frac{\gamma\hbar}{2}$ and $\beta = \frac{(1-3\cos^2\theta)}{r^3}$. To find the energy levels of these states, we must solve

$$|\langle\psi|\mathcal{H}|\psi\rangle - E\mathbf{1}| = 0. \tag{C.3}$$

If we use the substitutions

$$\begin{aligned}
a &= \alpha^2\beta \\
b &= \alpha(H_1-H_2) \\
\text{and } c &= \alpha(H_1+H_2),
\end{aligned}$$

we can expand Eq. (C.3) into

$$\begin{vmatrix}
-c+a-E & 0 & 0 & 0 \\
0 & -b-a-E & -a & 0 \\
0 & -a & b-a-E & 0 \\
0 & 0 & 0 & c+a-E
\end{vmatrix} = 0.$$

This equation is easily solved to give the eigen-energies

$$\begin{aligned}
E_+ &= -c+a \\
E_{0+} &= \sqrt{a^2+b^2}-a \\
E_{0-} &= -\sqrt{a^2+b^2}-a \\
E_- &= c+a,
\end{aligned}$$

which then lead to the eigenvectors

$$
\begin{aligned}
|\lambda_+\rangle &= |++\rangle \\
|\lambda_{0+}\rangle &= \frac{1}{\sqrt{2}\left(a^2+b^2+b\sqrt{a^2+b^2}\right)^{1/2}}\left[-a|+-\rangle+(b+\sqrt{a^2+b^2})|-+\rangle\right] \\
|\lambda_{0-}\rangle &= \frac{1}{\sqrt{2}\left(a^2+b^2-b\sqrt{a^2+b^2}\right)^{1/2}}\left[-a|+-\rangle+(b-\sqrt{a^2+b^2})|-+\rangle\right] \\
|\lambda_-\rangle &= |--\rangle.
\end{aligned}
$$

It will be useful to define

$$
\begin{aligned}
B_2 &= \frac{-a}{\sqrt{2}\left(a^2+b^2+b\sqrt{a^2+b^2}\right)^{1/2}} \\
C_2 &= \frac{b+\sqrt{a^2+b^2}}{\sqrt{2}\left(a^2+b^2+b\sqrt{a^2+b^2}\right)^{1/2}} \\
B_3 &= \frac{-a}{\sqrt{2}\left(a^2+b^2-b\sqrt{a^2+b^2}\right)^{1/2}} \\
C_3 &= \frac{b-\sqrt{a^2+b^2}}{\sqrt{2}\left(a^2+b^2-b\sqrt{a^2+b^2}\right)^{1/2}},
\end{aligned}
$$

which allows us to write

$$
\begin{aligned}
\lambda_{0+} &= B_2|+-\rangle + C_2|-+\rangle \\
\text{and } \lambda_{0-} &= B_3|+-\rangle + C_3|-+\rangle.
\end{aligned}
$$

The lines which will be observed will result from the following four transitions:

1. $|\lambda_+\rangle \leftrightarrow |\lambda_{0+}\rangle$

2. $|\lambda_+\rangle \leftrightarrow |\lambda_{0-}\rangle$

3. $|\lambda_{0+}\rangle \leftrightarrow |\lambda_{-}\rangle$

4. $|\lambda_{0-}\rangle \leftrightarrow |\lambda_{-}\rangle$.

The frequencies are given by:

$$\begin{aligned} h\nu_1 &= |E_+ - E_{0+}| &&= \left|-c + 2a - \sqrt{a^2+b^2}\right| \\ h\nu_2 &= |E_+ - E_{0-}| &&= \left|-c + 2a + \sqrt{a^2+b^2}\right| \\ h\nu_3 &= |E_{0+} - E_-| &&= \left|-c - 2a + \sqrt{a^2+b^2}\right| \\ h\nu_4 &= |E_{0-} - E_-| &&= \left|-c - 2a - \sqrt{a^2+b^2}\right| . \end{aligned}$$

If we wish to find the intensities of these lines, we will need to calculate the transition probabilities between the eigenstates of the system. To do this, we calculate the effect of inducing transitions by adding a rotating field in the xy plane. This is done by adding $\mathcal{H}' = -\gamma\hbar H_R(I_{1x} + I_{2x})$ to the Hamiltonian Eq. (C.2) (H_R is the magnitude of the rotating field).

In terms of I^+ and I_-,

$$\mathcal{H}' = -\frac{\gamma\hbar H_R}{2}\left(I_1^+ + I_1^- + I_2^+ + I_2^-\right)$$

so that

$$\begin{aligned} \mathcal{H}'|++\rangle &= -\frac{\gamma\hbar H_R}{2}(|-+\rangle + |+-\rangle) \\ \mathcal{H}'|--\rangle &= -\frac{\gamma\hbar H_R}{2}(|+-\rangle + |-+\rangle) \\ \mathcal{H}'[B_2|+-\rangle + C_2|-+\rangle] &= -\frac{\gamma\hbar H_R}{2}(B_2 + C_2)(|++\rangle + |--\rangle) \\ \mathcal{H}'[B_3|+-\rangle + C_3|-+\rangle] &= -\frac{\gamma\hbar H_R}{2}(B_3 + C_3)(|++\rangle + |--\rangle) . \end{aligned}$$

The transition matrix is then

$$\begin{array}{c} \\ \lambda_+ \\ \lambda_{0+} \\ \lambda_{0-} \\ \lambda_- \end{array} \begin{array}{c} \begin{array}{cccc} \lambda_+ & \lambda_{0+} & \lambda_{0-} & \lambda_- \end{array} \\ \begin{bmatrix} 0 & -\frac{\gamma\hbar H_R}{2}(B_2+C_2) & -\frac{\gamma\hbar H_R}{2}(B_3+C_3) & 0 \\ -\frac{\gamma\hbar H_R}{2}(B_2+C_2) & 0 & 0 & -\frac{\gamma\hbar H_R}{2}(B_2+C_2) \\ -\frac{\gamma\hbar H_R}{2}(B_3+C_3) & 0 & 0 & -\frac{\gamma\hbar H_R}{2}(B_3+C_3) \\ 0 & -\frac{\gamma\hbar H_R}{2}(B_2+C_2) & -\frac{\gamma\hbar H_R}{2}(B_3+C_3) & 0 \end{bmatrix} \end{array}.$$

Define

$$A_2 = -\frac{\gamma\hbar H_R}{2}(B_2+C_2)$$

$$\text{and } A_3 = -\frac{\gamma\hbar H_R}{2}(B_3+C_3).$$

Then the transition matrix becomes

$$\begin{bmatrix} 0 & A_2 & A_3 & 0 \\ A_2 & 0 & 0 & A_2 \\ A_3 & 0 & 0 & A_3 \\ 0 & A_2 & A_3 & 0 \end{bmatrix}.$$

The transition intensities are given by A_2^2 and A_3^2. Some simple algebraic manipulation gives

$$A_2^2 = \frac{\gamma^2\hbar^2 H_R^2}{4}\left(1 - a\frac{b+\sqrt{a^2+b^2}}{a^2+b^2+b\sqrt{a^2+b^2}}\right)$$

$$\text{and } A_3^2 = \frac{\gamma^2\hbar^2 H_R^2}{4}\left(1 - a\frac{b-\sqrt{a^2+b^2}}{a^2+b^2-b\sqrt{a^2+b^2}}\right).$$

We wish to normalize the intensities so that $A_2^2 + A_3^2 = 4$. Calculating $A_2^2 + A_3^2$ gives

$$A_2^2 + A_3^2 = \frac{\gamma^2\hbar^2 H_R^2}{2},$$

so we will have to multiply A_2 and A_3 by $\frac{2\sqrt{2}}{\gamma\hbar H_R}$. This gives the relative intensities of the transitions:

$$A_2^2 = \frac{\left(-a+b+\sqrt{a^2+b^2}\right)^2}{a^2+b^2+b\sqrt{a^2+b^2}}$$

$$\text{and } A_3^2 = \frac{\left(-a+b-\sqrt{a^2+b^2}\right)^2}{a^2+b^2-b\sqrt{a^2+b^2}}.$$

The final results are (for frequencies in units of $1/h$):

frequency		*intensity*
$h\nu = c+2a+\sqrt{a^2+b^2}$		$\frac{\left(-a+b-\sqrt{a^2+b^2}\right)^2}{a^2+b^2-b\sqrt{a^2+b^2}}$
$h\nu = c-2a-\sqrt{a^2+b^2}$		
$h\nu = c+2a-\sqrt{a^2+b^2}$		$\frac{\left(-a+b+\sqrt{a^2+b^2}\right)^2}{a^2+b^2+b\sqrt{a^2+b^2}}$.
$h\nu = c-2a+\sqrt{a^2+b^2}$		

We will wish to use these results with the positions in units of gauss, so the results are:

position		*intensity*
$h = c+2a+\sqrt{a^2+b^2}$		$\frac{\left(-a+b-\sqrt{a^2+b^2}\right)^2}{a^2+b^2-b\sqrt{a^2+b^2}}$
$h = c-2a-\sqrt{a^2+b^2}$		
$h = c+2a-\sqrt{a^2+b^2}$		$\frac{\left(-a+b+\sqrt{a^2+b^2}\right)^2}{a^2+b^2+b\sqrt{a^2+b^2}}$.
$h = c-2a+\sqrt{a^2+b^2}$		

Here, h is the position of the line, and a, b, c are redefined as:

$$\begin{aligned} a &= \frac{1}{4}\gamma_H \hbar \beta \\ b &= \frac{1}{2}(H_1 - H_2) \\ \text{and } c &= \frac{1}{2}(H_1 + H_2). \end{aligned}$$

Appendix D

Derivation of the magnetic moment

We wish to find the time averaged magnetic moment of a spin system with a Hamiltonian of the form

$$\mathcal{H} = -\sum_i \beta \mathbf{S}_i \cdot \mathbf{g} \cdot \mathbf{H}_0 - J \sum_i \mathbf{S}_i \cdot \mathbf{S}_{i+1} + D \sum_i S_{iz}^2.$$

For $CsFeCl_3 \cdot 2H_2O$, the observed values of J and D make the high temperature approximation ($\frac{\mathcal{H}}{kT} \ll 1$) a borderline assumption. To avoid any problems with truncation of the power series expansion in $\frac{1}{kT}$, we will use the following derivation to find the moment. This allows us to avoid truncating the power series before it would be correct to do so. To begin, we have

$$\overline{\mu}_k = \frac{Tr\{\beta \mathbf{g}_k \cdot \mathbf{S}_k \rho\}}{Tr\{\rho\}}, \tag{D.1}$$

where $\rho = e^{-\frac{\mathcal{H}}{kT}}$ ($\mathbf{g}_k$ is a third rank tensor). Consider the following three power series:

$$A(x) = A_0 + A_1 x + A_2 x^2 + \ldots = A(0) + \left.\frac{\partial A}{\partial x}\right|_0 x + \left.\frac{\partial^2 A}{\partial x^2}\right|_0 x^2 + \ldots$$

$$B(x) = B_0 + B_1 x + B_2 x^2 + \ldots = B(0) + \left.\frac{\partial B}{\partial x}\right|_0 x + \left.\frac{\partial^2 B}{\partial x^2}\right|_0 x^2 + \ldots$$

$$C(x) = C_0 + C_1 x + C_2 x^2 + \ldots = C(0) + \left.\frac{\partial C}{\partial x}\right|_0 x + \left.\frac{\partial^2 C}{\partial x^2}\right|_0 x^2 + \ldots,$$

where we are going to use $x = \frac{1}{kT}$. If we let $A(x)$ be the numerator of Eq. (D.1), $B(x)$ the denominator, and $C(x) = \overline{\mu}_k$, then

$$C(x) = \frac{A(x)}{B(x)}.$$

We can immediately see that

$$\begin{aligned} C_0 &= C(0) = \frac{A(0)}{B(0)} = \frac{A_0}{B_0}, \\ C_1 &= \left.\frac{\partial C}{\partial x}\right|_0 = \left.\frac{\partial (AB^{-1})}{\partial x}\right|_0 = \frac{A_1 B_0 - A_0 B_1}{B_0^2}, \end{aligned}$$

and

$$\begin{aligned} C_2 &= \frac{1}{2}\left.\frac{\partial^2 C}{\partial x^2}\right|_0 = \frac{1}{2}\frac{\partial}{\partial x}\left(\frac{\partial A}{\partial x}\frac{1}{B} - \frac{A}{B^2}\frac{\partial B}{\partial x}\right)\Bigg|_0 \\ &= \frac{1}{2}\left[\frac{1}{B}\frac{\partial^2 A}{\partial x^2} - \frac{1}{B^2}\frac{\partial A}{\partial x}\frac{\partial B}{\partial x} - \frac{1}{B^2}\frac{\partial A}{\partial x}\frac{\partial B}{\partial x} + 2\frac{A}{B^3}\left(\frac{\partial B}{\partial x}\right)^2 - \frac{A}{B^2}\frac{\partial^2 B}{\partial x^2}\right]_0 \\ &= \frac{A_2}{B_0} - \frac{A_1 B_1}{B_0^2} + \frac{A_0 B_1^2}{B_0^3} - \frac{A_0 B_2}{B_0^2}. \end{aligned}$$

First, we will find the coefficients of $A(x)$:

$$\begin{aligned} A(x) &= Tr\left\{\beta \mathbf{g}_k \cdot \mathbf{S}_k e^{-\frac{\mathcal{H}}{kT}}\right\} \\ &= \beta \mathbf{g}_k \cdot Tr\left\{\mathbf{S}_k e^{-\frac{\mathcal{H}}{kT}}\right\} \\ &= \beta \mathbf{g}_k \cdot Tr\left\{\mathbf{S}_k - \frac{\mathbf{S}_k \mathcal{H}}{kT} + \frac{1}{2k^2T^2}\mathbf{S}_k \mathcal{H}^2 - \ldots\right\} \end{aligned}$$

$$= \beta \mathbf{g}_k \cdot Tr\{\mathbf{S}_k\} - \frac{\beta}{kT} \mathbf{g}_k \cdot Tr\{\mathbf{S}_k \mathcal{H}\} + \frac{\beta}{2k^2T^2} \mathbf{g}_k \cdot Tr\left\{\mathbf{S}_k \mathcal{H}^2\right\} - \ldots .$$

If we make the substitution $x = \frac{1}{kT}$ then we have the coefficients :

$$\begin{aligned} A_0 &= \beta \mathbf{g} \cdot Tr\{\mathbf{S}_k\} \\ A_1 &= -\beta \mathbf{g}_k \cdot Tr\{\mathbf{S}_k \mathcal{H}\} \\ A_2 &= \beta \mathbf{g}_k \cdot \frac{1}{2} Tr\left\{\mathbf{S}_k \mathcal{H}^2\right\}. \end{aligned} \tag{D.2}$$

Next, we will find the coefficients of $B(x)$:

$$\begin{aligned} B(x) &= Tr\{\rho\} = Tr\left\{e^{-\frac{\mathcal{H}}{kT}}\right\} = Tr\left\{1 - \frac{\mathcal{H}}{kT} + \frac{\mathcal{H}^2}{2k^2T^2} - \ldots\right\} \\ &= Tr\{1\} - \frac{1}{kT} Tr\{\mathcal{H}\} + \frac{1}{2k^2T^2} Tr\left\{\mathcal{H}^2\right\} + \ldots . \end{aligned}$$

Again, we will use the substitution $x = \frac{1}{kT}$ to obtain the coefficients for $B(x)$:

$$\begin{aligned} B_0 &= Tr\{1\} \\ B_1 &= -Tr\{\mathcal{H}\} \\ B_2 &= \frac{1}{2} Tr\left\{\mathcal{H}^2\right\}. \end{aligned} \tag{D.3}$$

This leads to a number of traces which must be evaluated. To begin, there are N spins, each of which has $(2S + 1)$ states, so

$$Tr\{1\} = (2S + 1)^N. \tag{D.4}$$

Next, we have that

$$Tr\{\mathbf{S}_k\} = 0. \tag{D.5}$$

This is because for every non-zero positive eigenvalue of $\mathbf{S}_k$, there is a corresponding negative eigenvalue which combines to give zero. This same symmetry argument applies for any trace of an odd power of $\mathbf{S}_k$.

Then

$$\begin{aligned} Tr\{\mathcal{H}\} &= -\beta\sum_i Tr\{\mathbf{S}_i\}\cdot\mathbf{g}_i\cdot\mathbf{H}_0 - J\sum_i Tr\{\mathbf{S}_i\cdot\mathbf{S}_{i+1}\} + D\sum_i Tr\left\{\mathbf{S}_{iz}^2\right\} \\ &= D\sum_i Tr\left\{\mathbf{S}_{iz}^2\right\} \\ &= \frac{1}{3}DNS(S+1)(2S+1)^N \end{aligned} \tag{D.6}$$

because

- $Tr\{\mathbf{S}_i\cdot\mathbf{S}_{i+1}\} = 0$ by symmetry because (obviously) $i \neq i+1$
- $Tr\{S_{iz}^2\} = \frac{1}{3}S(S+1)(2S+1)^N$.

The second statement follows because $Tr_i\{S_{iz}^2\} = \frac{1}{3}Tr_i\{S_i^2\}$, where $Tr_i\{\}$ means that we are taking a trace only over quantum states of spin i. There are $(2S+1)$ diagonal elements of $Tr_i\{S_i^2\}$, each of magnitude $S(S+1)$, which gives $Tr_i\{S_{iz}\} = \frac{1}{3}S(S+1)(2S+1)$. Expanding Tr_i over all i gives $N-1$ terms $= (2S+1)$, and everything is repeated for all N terms, giving $Tr\{S_{iz}^2\} = \frac{1}{3}S(S+1)(2S+1)^N$.

Next, for $Tr\{\mathbf{S}_k\mathcal{H}\}$ we have

$$\begin{aligned} Tr\{\mathbf{S}_k\mathcal{H}\} &= Tr\left\{\mathbf{S}_k\left(-\sum_i \beta\mathbf{S}_i\cdot\mathbf{g}_i\cdot\mathbf{H}_0 - J\sum_i \mathbf{S}_i\cdot\mathbf{S}_{i+1} + D\sum_i S_{iz}^2\right)\right\} \\ &= -\beta\sum_i Tr\{\mathbf{S}_k\mathbf{S}_i\}\cdot\mathbf{g}_i\cdot\mathbf{H}_0 - J\sum_i Tr\{\mathbf{S}_k\mathbf{S}_i\cdot\mathbf{S}_{i+1}\} + D\sum_i Tr\left\{\mathbf{S}_k S_{iz}^2\right\} \\ &= -\beta Tr\{\mathbf{S}_k\mathbf{S}_k\}\cdot\mathbf{g}_k\cdot\mathbf{H}_0 \\ &= -\beta\frac{1}{3}Tr\left\{S_k^2\right\}\mathbf{u}\cdot\mathbf{g}_k\cdot\mathbf{H}_0 \\ &= -\beta\frac{1}{3}S(S+1)(2S+1)^N\mathbf{g}_k\cdot\mathbf{H}_0, \end{aligned} \tag{D.7}$$

where

- $\mathbf{u} = \hat{\mathbf{i}}\hat{\mathbf{i}} + \hat{\mathbf{j}}\hat{\mathbf{j}} + \hat{\mathbf{k}}\hat{\mathbf{k}}$ is the unit dyad,
- $S_k^2 = S_{kx}^2 + S_{ky}^2 + S_{kz}^2$,
- $Tr\{S_k^2\} = S(S+1)(2S+1)^N$.

Finally, to find $Tr\{\mathbf{S}_k\mathcal{H}^2\}$, we have that

$$
\begin{aligned}
Tr\Big\{\mathbf{S}_k\mathcal{H}^2\Big\} &= Tr\left\{\mathbf{S}_k\left(-\sum_i \beta\mathbf{S}_i\cdot\mathbf{g}_i\cdot\mathbf{H}_0 - J\sum_i \mathbf{S}_i\cdot\mathbf{S}_{i+1} + D\sum_i S_{iz}^2\right)^2\right\} \\
&= Tr\left\{\mathbf{S}_k\sum_i(\beta\mathbf{S}_i\cdot\mathbf{g}_i\cdot\mathbf{H}_0)\sum_j(\beta\mathbf{S}_j\cdot\mathbf{g}_j\cdot\mathbf{H}_0)\right\} \\
&\quad + Tr\left\{\mathbf{S}_k J\sum_i(\mathbf{S}_i\cdot\mathbf{S}_{i+1})J\sum_j \mathbf{S}_j\cdot\mathbf{S}_{j+1}\right\} \\
&\quad + Tr\left\{\mathbf{S}_k D\sum_i S_{iz}^2 D\sum_j S_{jz}^2\right\} \\
&\quad + Tr\left\{\mathbf{S}_k\sum_i(-\beta\mathbf{S}_i\cdot\mathbf{g}_i\cdot\mathbf{H}_0)(-J)\sum_j \mathbf{S}_j\cdot\mathbf{S}_{j+1}\right\} \\
&\quad + Tr\left\{\mathbf{S}_k(-J)\sum_i S_{iz}^2\sum_j(-\beta\mathbf{S}_j\cdot\mathbf{g}_j\cdot\mathbf{H}_0)\right\} \\
&\quad + Tr\left\{\mathbf{S}_k\sum_i(-\beta\mathbf{S}_i\cdot\mathbf{g}_i\cdot\mathbf{H}_0)D\sum_j S_{jz}^2\right\} \\
&\quad + Tr\left\{\mathbf{S}_k D\sum_i S_{iz}^2\sum_j(-\beta\mathbf{S}_j\cdot\mathbf{g}_j\cdot\mathbf{H}_0)\right\} \\
&\quad + Tr\left\{\mathbf{S}_k(-J\sum_i \mathbf{S}_i\cdot\mathbf{S}_{i+1})D\sum_j S_{jz}^2\right\}
\end{aligned}
$$

$$+ Tr\left\{ \mathbf{S}_k D \sum_i S_{iz}^2 (-J) \sum_j \mathbf{S}_j \cdot \mathbf{S}_{j+1} \right\} .$$

The first term is $\beta^2 \sum_i \sum_j Tr\{\mathbf{S}_k(\mathbf{S}_i \cdot \mathbf{g}_i \cdot \mathbf{H}_0)(\mathbf{S}_j \cdot \mathbf{g}_j \cdot \mathbf{H}_0)\} = 0$ by symmetry (everything $\mathcal{O}(S^3)$).

The next two terms are both equal to zero because any value for i, j, or k leads to a case of odd symmetry in S.

For the fourth and fifth terms everything equals zero, except when the following four cases are true :

1. $j = k$ and $i = k + 1$
2. $j + 1 = k$ and $i = k - 1$
3. $i = 1$ and $j = k + 1$
4. $i + 1 = k$ and $j = k - 1$.

These cases combine to give

$$\begin{aligned} & Tr\{\mathbf{S}_k(-\beta \mathbf{S}_{k+1} \cdot \mathbf{g}_{k+1} \cdot \mathbf{H}_0)(-J\mathbf{S}_k \cdot \mathbf{S}_{k+1})\} + Tr\{\mathbf{S}_k(-J)\mathbf{S}_k \cdot \mathbf{S}_{k+1}(-\beta \mathbf{S}_{k+1} \cdot \mathbf{g}_{k+1} \cdot \mathbf{H}_0)\} \\ & \quad + Tr\{\mathbf{S}_k(-\beta \mathbf{S}_{k-1} \cdot \mathbf{g}_{k-1} \cdot \mathbf{H}_0)(-J\mathbf{S}_{k-1} \cdot \mathbf{S}_k)\} + Tr\{\mathbf{S}_k(-J)\mathbf{S}_{k-1} \cdot \mathbf{S}_k(-\beta \mathbf{S}_{k-1} \cdot \mathbf{g}_{k-1} \cdot \mathbf{H}_0)\} \\ = \; & \beta J \left[Tr\{\mathbf{S}_k(\mathbf{S}_k \cdot \mathbf{S}_{k+1})\mathbf{S}_{k+1}\} \cdot \mathbf{g}_{k+1} \cdot \mathbf{H}_0 + Tr\{\mathbf{S}_k(\mathbf{S}_k \cdot \mathbf{S}_{k+1})\mathbf{S}_{k+1}\} \cdot \mathbf{g}_{k+1} \cdot \mathbf{H}_0 \right. \\ & \quad \left. + Tr\{\mathbf{S}_{k-1}(\mathbf{S}_{k-1} \cdot \mathbf{S}_k)\mathbf{S}_k\} \cdot \mathbf{g}_{k-1} \cdot \mathbf{H}_0 + Tr\{\mathbf{S}_{k-1}(\mathbf{S}_{k-1} \cdot \mathbf{S}_k)\mathbf{S}_k\} \cdot \mathbf{g}_{k-1} \cdot \mathbf{H}_0 \right] . \end{aligned}$$

Consider

$$\begin{aligned} & Tr\{\mathbf{S}_k(\mathbf{S}_k \cdot \mathbf{S}_{k+1})\mathbf{S}_{k+1}\} \\ & = \sum_{m_1, m_2, \ldots} \langle m_1 m_2 \ldots | \mathbf{S}_k(\mathbf{S}_k \cdot \mathbf{S}_{k+1})\mathbf{S}_{k+1} | m_1 m_2 \ldots \rangle \end{aligned}$$

$$
\begin{aligned}
&= \sum_{m_1}\langle m_1|m_1\rangle \ldots \sum_{m_k}\langle m_k|\mathbf{S}_k\mathbf{S}_k|m_k\rangle \cdot \sum_{m_{k+1}}\langle m_{k+1}|\mathbf{S}_{k+1}\mathbf{S}_{k+1}|m_{k+1}\rangle \ldots \sum_{m_N}\langle m_N|m_N\rangle \\
&= (2S+1)^{N-2}\left(Tr_k\left\{S_{kx}^2\right\}\hat{\imath}\hat{\imath} + Tr_k\left\{S_{ky}^2\right\}\hat{\jmath}\hat{\jmath} + Tr_k\left\{S_{kz}^2\right\}\hat{\mathbf{k}}\hat{\mathbf{k}}\right) \\
&\quad \cdot \left(Tr_{(k+1)x}\left\{S_{(k+1)x}^2\right\}\hat{\imath}\hat{\imath} + Tr_{k+1}\left\{S_{(k+1)x}^2\right\}\hat{\jmath}\hat{\jmath} + Tr_{k+1}\left\{S_{(k+1)z}^2\right\}\hat{\mathbf{k}}\hat{\mathbf{k}}\right) \\
&= (2S+1)^{N-2}\frac{1}{3}\left(Tr_k\left\{S_k^2\right\}\mathbf{u}\right)\cdot\frac{1}{3}\left(Tr_{k+1}\left\{S_{k+1}^2\right\}\mathbf{u}\right) \\
&= \frac{1}{9}(2S+1)^{N-2}S^2(S+1)^2(2S+1)^2\mathbf{u} \\
&= \frac{1}{9}S^2(S+1)^2(2S+1)^N\mathbf{u}.
\end{aligned}
$$

To return to the fourth and fifth terms:

$$
\begin{aligned}
&= \frac{2}{9}\beta J\left[S^2(S+1)^2(2S+1)^N\mathbf{g}_{k+1}\cdot\mathbf{H}_0 + S^2(S+1)^2(2S+1)^N\mathbf{g}_{k-1}\cdot\mathbf{H}_0\right] \\
&= \frac{2}{9}\beta J S^2(S+1)^2(2S+1)^N(\mathbf{g}_{k+1}+\mathbf{g}_{k-1})\cdot\mathbf{H}_0.
\end{aligned}
$$

The sixth and seventh terms are all= 0 except where $i = k$ or $j = k$. The non-zero remainder is:

$$
\begin{aligned}
&= -\beta D\left[Tr\left\{\mathbf{S}_k(\mathbf{S}_k\cdot\mathbf{g}_k\cdot\mathbf{H}_0)\sum_j S_{jz}^2\right\} + Tr\left\{\mathbf{S}_k\sum_i \mathbf{S}_{iz}^2(\mathbf{S}_k\cdot\mathbf{g}_k\cdot\mathbf{H}_0)\right\}\right] \\
&= -\beta D\left[Tr\left\{\sum_j \mathbf{S}_{jz}^2\mathbf{S}_k\mathbf{S}_k\right\} + Tr\left\{\mathbf{S}_k\sum_i S_{iz}^2\mathbf{S}_k\right\}\right]\cdot\mathbf{g}_k\cdot\mathbf{H}_0 \\
&= -2\beta D Tr\left\{\sum_j S_{jz}^2\mathbf{S}_k\mathbf{S}_k\right\}\cdot\mathbf{g}_k\cdot\mathbf{H}_0 \\
&= -2\beta D\sum_j Tr\left\{S_{jz}^2\mathbf{S}_k\mathbf{S}_k\right\}\cdot\mathbf{g}_k\cdot\mathbf{H}_0. \qquad \text{(D.8)}
\end{aligned}
$$

Consider $Tr\left\{S_{jz}^2 \mathbf{S}_k \mathbf{S}_k\right\}$: For each $j \neq k$

$$\begin{aligned} Tr\left\{S_{jz}^2 \mathbf{S}_k \mathbf{S}_k\right\} &= (2S+1)^{N-2} Tr_j\left\{S_{jz}^2\right\} \frac{1}{3} Tr_k\left\{S_k^2\right\} \mathbf{u} \\ &= \frac{1}{9} S^2(S+1)^2(2S+1)^N \mathbf{u}. \end{aligned} \tag{D.9}$$

For $j = k$

$$\begin{aligned} & Tr\left\{S_{jz}^2 \mathbf{S}_k \mathbf{S}_k\right\} \\ &= Tr\left\{S_{kz}^2 \mathbf{S}_k \mathbf{S}_k\right\} \\ &= (2S+1)^{N-1} Tr_k\left\{S_{kz}^2 \mathbf{S}_k \mathbf{S}_k\right\} \\ &= (2S+1)^{N-1}\left[Tr_k\left\{S_{kz}^2 S_{kx}^2\right\} \hat{\mathbf{i}}\hat{\mathbf{i}} + Tr_k\left\{S_{kz}^2 S_{ky}^2\right\} \hat{\mathbf{j}}\hat{\mathbf{j}} + Tr_k\left\{S_{kz}^4\right\} \hat{\mathbf{k}}\hat{\mathbf{k}}\right] \\ &= (2S+1)^N\left[\left(\frac{1}{15} S^2(S+1)^2 + \frac{1}{30} S(S+1)\right)(\hat{\mathbf{i}}\hat{\mathbf{i}} + \hat{\mathbf{j}}\hat{\mathbf{j}})\right. \\ &\quad \left. + \left(\frac{1}{5} S^2(S+1)^2 - \frac{1}{15} S(S+1)\right) \hat{\mathbf{k}}\hat{\mathbf{k}}\right] \\ &= \frac{1}{5} S(S+1)(2S+1)^N\left[\left(\frac{1}{3} S(S+1) + \frac{1}{6}\right)(\hat{\mathbf{i}}\hat{\mathbf{i}} + \hat{\mathbf{j}}\hat{\mathbf{j}}) + \left(S(S+1) - \frac{1}{3}\right) \hat{\mathbf{k}}\hat{\mathbf{k}}\right] \end{aligned} \tag{D.10}$$

where we have used the facts that

$$Tr_k\left\{S_{kz}^2 S_{kx}^2\right\} = Tr_k\left\{S_{kz}^2 S_{ky}^2\right\} = (2S+1)\left(\frac{1}{15} S^2(S+1)^2 + \frac{1}{30} S(S+1)\right)$$

and

$$Tr_k\left\{S_{kz}^4\right\} = (2S+1)\left(\frac{1}{5} S^2(S+1)^2 - \frac{1}{15} S(S+1)\right).$$

There are $N-1$ terms where $j \neq k$, and one term where $j = k$. If we now substitute $N-1$ times Eq. (D.9) plus Eq. (D.10) into Eq. (D.8), we have the fifth

and sixth terms:

$$
\begin{aligned}
&= -2\beta D\left\{(N-1)\frac{1}{9}S^2(S+1)^2(2S+1)^N\mathbf{u}+\frac{1}{5}S(S+1)(2S+1)^N\right.\\
&\quad\left.\left[\left(\frac{1}{3}S(S+1)+\frac{1}{6}\right)(\hat{\imath}\hat{\imath}+\hat{\jmath}\hat{\jmath})+\left(S(S+1)-\frac{1}{3}\right)\hat{\mathbf{k}}\hat{\mathbf{k}}\right]\right\}\cdot\mathbf{g}_k\cdot\mathbf{H}_0\\
&= -\frac{2}{3}\beta DS(S+1)(2S+1)^N\left\{\frac{1}{3}(N-1)S(S+1)\mathbf{u}+\right.\\
&\quad\left.\frac{1}{5}\left[\left(S(S+1)+\frac{1}{2}\right)(\hat{\imath}\hat{\imath}+\hat{\jmath}\hat{\jmath})+(3S(S+1)-1)\hat{\mathbf{k}}\hat{\mathbf{k}}\right]\right\}\cdot\mathbf{g}_k\mathbf{H}_0.
\end{aligned}
$$

The last two terms are equal to zero by symmetry.

Gathering all of the above terms together, we have

$$
\begin{aligned}
&Tr\left\{\mathbf{S}_k\mathcal{H}^2\right\}\\
&= \frac{2}{9}\beta JS^2(S+1)^2(2S+1)^N(\mathbf{g}_{k+1}+\mathbf{g}_{k-1})\cdot\mathbf{H}_0-\frac{2}{3}\beta DS(S+1)(2S+1)^N\\
&\quad\times\left\{\frac{1}{3}(N-1)S(S+1)\mathbf{u}+\frac{1}{5}\left[\left(S(S+1)+\frac{1}{2}\right)(\hat{\imath}\hat{\imath}+\hat{\jmath}\hat{\jmath})\right.\right.\\
&\quad\left.\left.+(3S(S+1)-1)\hat{\mathbf{k}}\hat{\mathbf{k}}\right]\right\}\cdot\mathbf{g}_k\cdot\mathbf{H}_0\\
&= \frac{2}{3}\beta S(S+1)(2S+1)^N\left\{\frac{1}{3}JS(S+1)(\mathbf{g}_{k+1}+\mathbf{g}_{k-1})-D\left[\frac{1}{3}(N-1)S(S+1)\mathbf{u}\right.\right.\\
&\quad\left.\left.+\frac{1}{5}\left(S(S+1)+\frac{1}{2}\right)(\hat{\imath}\hat{\imath}+\hat{\jmath}\hat{\jmath})+\frac{1}{5}(3S(S+1)-1)\hat{\mathbf{k}}\hat{\mathbf{k}}\right]\cdot\mathbf{g}_k\right\}\cdot\mathbf{H}_0. \qquad \text{(D.11)}
\end{aligned}
$$

Substituting Eq. (D.5), Eq. (D.7), and Eq. (D.11) into Eq. (D.2) we have:

$$
\begin{aligned}
A_0 &= 0\\
A_1 &= \frac{1}{3}\beta^2S(S+1)(2S+1)^N\mathbf{g}_k\cdot\mathbf{g}_k\cdot\mathbf{H}_0\\
A_2 &= \frac{1}{3}\beta^2S(S+1)(2S+1)^N\mathbf{g}_k\cdot\left\{\frac{1}{3}S(S+1)\left[(J\mathbf{g}_{k+1}-D(N=1)\mathbf{g}_k+J\mathbf{g}_{k-1})\right]\right.
\end{aligned}
$$

$$-\frac{1}{5}D\left[\left(S(S+1)+\frac{1}{2}\right)(\hat{\imath}\hat{\imath}+\hat{\jmath}\hat{\jmath})+(3S(S+1)-1)\hat{\mathbf{k}}\hat{\mathbf{k}}\right]\cdot\mathbf{g}_k\Big\}\cdot\mathbf{H}_0. \qquad \text{(D.12)}$$

Substituting Eq. (D.4) and Eq. (D.6) into Eq. (D.3) we have:

$$\begin{aligned} B_0 &= (2S+1)^N \\ B_1 &= -\frac{1}{3}DNS(S+1)(2S+1)^N, \end{aligned} \qquad \text{(D.13)}$$

where we have anticipated $A_0 = 0$, so we will not need B_2 to find the first three terms of $C(x)$. Using Eq. (D.12) and Eq. (D.13) we find $C(x)$:

$$\begin{aligned} C_0 &= \frac{A_0}{B_0} = 0, \\ C_1 &= \frac{A_1B_0 - A_0B_1}{B_0^2} = \frac{1}{3}\beta^2 S(S+1)\mathbf{g}_k\cdot\mathbf{g}_k\cdot\mathbf{H}_0, \\ C_2 &= \frac{A_2}{B_0} - \frac{A_1B_1}{B_0^2} + \frac{A_0B_1^2}{B_0^3} - \frac{A_0B_2}{B_0^2} = \frac{A_2B_0 - A_1B_1}{B_0^2} \\ &= \frac{1}{3}\beta^2 S(S+1)\mathbf{g}_k\cdot\Big\{\frac{1}{3}S(S+1)(J\mathbf{g}_{k-1}+D\mathbf{g}_k+J\mathbf{g}_{k+1}) \\ &\quad -\frac{1}{5}D\left[\left(S(S+1)+\frac{1}{2}\right)(\hat{\imath}\hat{\imath}+\hat{\jmath}\hat{\jmath})+(3S(S+1)-1)\hat{\mathbf{k}}\hat{\mathbf{k}}\right]\cdot\mathbf{g}_k\Big\}\cdot\mathbf{H}_0. \end{aligned}$$

This leads us finally to

$$\begin{aligned} \overline{\mu_k} &= C\left(\frac{1}{kT}\right) \\ &= C_0 + C_1\frac{1}{kT} + C_2\frac{1}{k^2T^2} + \ldots \\ &= \frac{\beta^2}{3kT}S(S+1)\mathbf{g}_k\cdot\mathbf{g}_k\cdot\mathbf{H}_0 \\ &\quad + \frac{\beta^2}{3k^2T^2}S(S+1)\mathbf{g}_k\cdot\Big\{\frac{1}{3}S(S+1)(J\mathbf{g}_{k-1}+D\mathbf{g}_k+J\mathbf{g}_{k+1}) \\ &\quad -\frac{1}{5}D\left[\left(S(S+1)+\frac{1}{2}\right)(\hat{\imath}\hat{\imath}+\hat{\jmath}\hat{\jmath})+(3S(S+1)-1)\hat{\mathbf{k}}\hat{\mathbf{k}}\right]\cdot\mathbf{g}_k\Big\}\cdot\mathbf{H}_0+\ldots. \end{aligned}$$